water

MDPI

Article

Geoelectric Monitoring of the Electric Potential Field of the Lower Rio Grande before, during, and after Intermittent Streamflow, May–October, 2022

Scott J. Ikard [1,*], Kenneth C. Carroll [2], Dale F. Rucker [3], Andrew P. Teeple [1], Chia-Hsing Tsai [2], Jason D. Payne [1], Erek H. Fuchs [4] and Ahsan Jamil [2]

[1] U.S. Geological Survey, Oklahoma Texas Water Science Center, Austin, TX 78754, USA; efuchs@ebid-nm.org.com (A.P.T.)
[2] College of Agricultural, Consumer and Environmental Sciences, New Mexico State University, Las Cruces, NM 88003-8003, USA; kccarr@nmsu.edu (K.C.C.)
[3] hydroGEOPHYSICS, Inc., 3450 South Broadmont Drive, Tucson, AZ 85713, USA; drucker@hgiworld.com
[4] Elephant Butte Irrigation District, 530 South Melendres Street, Las Cruces, NM 88005, USA
* Correspondence: sikard@usgs.gov

Abstract: Understanding the intermittent hydraulic connectivity between ephemeral streams and alluvial aquifers is a key challenge for managing water resources in arid environments. The lower Rio Grande flows for short, discontinuous periods during the irrigation season through the Mesilla Basin in southeastern New Mexico and southwestern Texas. Hydraulic connections between the Rio Grande and the Rio Grande alluvial aquifer in the Mesilla Basin vary spatially and temporally and are not well understood. Self-potential (SP) monitoring and time-lapse electric resistivity tomography (ERT) were therefore performed along linear cross-sections spanning the riverbed and flood plain for more than 4 months to monitor the transient hydraulic connection between the river and the alluvial aquifer by measuring time-lapse changes in the electric potential field in the riverbed and flood plain. The monitoring period began on 21 May 2022, when the riverbed was completely dry, continued through the irrigation season while streamflow was provided by reservoir releases from upstream dams, and ended on 4 October 2022, when the riverbed was again dry. SP monitoring data show (1) a background condition in the dry riverbed consisting of (a) a positive electric potential anomaly with a maximum amplitude of about +100 mV attributed predominantly to a subsurface vertical salt concentration gradient and (b) diurnal electric potential fluctuations with amplitudes of 40,000–90,000 mV attributed to near-surface heat conduction driven by weather variability, in addition to (2) a streaming potential anomaly during the irrigation season with a maximum amplitude of about −3500 mV whose transient behavior clearly exhibited a change from the background anomaly to depict exclusively losing streamflow conditions that persisted through the irrigation season. Time-lapse ERT monitoring results depict rapid infiltration of streamflow into the subsurface and imply the river and Rio Grande alluvial aquifer established a full hydraulic connection within a few hours after streamflow arrival at the monitoring site. SP monitoring data show an apparent transition from hydraulic connection to disconnection at the end of the irrigation season and indicate that the transitional phase between connection and disconnection may last substantially longer than the transition from disconnection to connection. The combination of SP and ERT monitoring demonstrated herein shows the potential for broader applications of time-lapse monitoring of hydraulic intermittency and near-surface heat fluxes in different rivers.

Keywords: self-potential; resistivity; Rio Grande; river; climate; groundwater; surface-water; groundwater–surface-water exchange; heat conduction; monitoring

Citation: Ikard, S.J.; Carroll, K.C.; Rucker, D.F.; Teeple, A.P.; Tsai, C.-H.; Payne, J.D.; Fuchs, E.H.; Jamil, A. Geoelectric Monitoring of the Electric Potential Field of the Lower Rio Grande before, during, and after Intermittent Streamflow, May–October, 2022. *Water* **2023**, *15*, 1652. https://doi.org/10.3390/w15091652

Academic Editor: Serban Danielescu

Received: 8 March 2023
Revised: 17 April 2023
Accepted: 19 April 2023
Published: 23 April 2023

Copyright: © 2023 by the authors. Licensee MDPI, Basel, Switzerland. This article is an open access article distributed under the terms and conditions of the Creative Commons Attribution (CC BY) license (https://creativecommons.org/licenses/by/4.0/).

1. Introduction

Understanding the complexity of hydraulic connections between rivers and alluvial aquifers is one of the key challenges of managing surface-water (SW) and groundwater (GW) resources [1–6]. For example, GW withdrawals from a flood plain for agricultural irrigation may capture and deplete SW from a river as drawdown cones migrate outward from the pumping wells and intersect the river, thereby reducing streamflow rates. The streamflow that is thus lost from the river may have previously been appropriated through SW rights or legally mandated to remain as streamflow for ecological conservation (i.e., minimum flow requirements). Managing SW and GW resources to meet the needs of all stakeholders is challenging because rivers exhibit spatiotemporal variability in hydraulic connection to alluvial aquifers and oscillate between gaining or losing conditions. Overcoming these challenges to better understand the spatiotemporal changes in river–aquifer hydraulic connectivity therefore requires knowledge of the spatial distribution of hydraulic connection and directions (SW gain or loss), rates of water transfer between the river and aquifer (referred to herein as "SW–GW exchange"), and how the processes vary through time [7].

The geomorphology (alluvial versus bedrock riverbed) and streamflow characteristics (perennial versus ephemeral streamflow) of the river exacerbate the challenges associated with managing SW and GW resources. Perennial rivers convey streamflow continuously such that the SW in the river and GW underlying the riverbed in the alluvium and flood plain sediments (i.e., the "alluvial aquifer") are a single interconnected resource [8,9]. In contrast, ephemeral rivers convey intermittent streamflow such that the hydraulic connection between the river and alluvial aquifer is intermittent, occurring during periods of streamflow and possibly varying temporally and spatially while streamflow is conveyed [10–13]. Whether perennial or ephemeral, peak streamflow conditions cause river stages to rise and alter hydraulic gradients between the river and any aquifers connected to the river. Recharge to aquifers occurs when SW flows from the river channel through the riverbed and into the underlying sediments and rocks that contain hydraulically connected aquifers. During periods of drought, streamflow is either sustained by base flow originating from underlying aquifers or the river dries up as hydraulic heads and GW levels decline in the aquifer and SW is lost from the riverbed as surficial infiltration or evaporates into the atmosphere [10–13].

Four distinct states of hydraulic connection between a river and an alluvial aquifer are illustrated and described by [6]. The four states of hydraulic connection include (1) gaining and (2) losing conditions in the hydraulically connected state, (3) a transitional state between hydraulically connected and disconnected, and (4) the disconnected state. A natural channel conveying streamflow is hydraulically connected to an alluvial aquifer when the elevation of the phreatic surface in the alluvial aquifer exceeds the riverbed elevation and coincides with the elevation of the water in the river [6]. In a hydraulically connected river–alluvial aquifer system, the river gains or loses SW through the riverbed and banks depending upon the river stage and the hydraulic head distribution within the alluvial aquifer [3]. In the gaining connected system, the hydraulic head in the aquifer is greater than the hydraulic head supplied by the river, whereas in a losing connected system, the hydraulic head in the aquifer is less than the hydraulic head supplied by the river, and the rate of loss is predominantly controlled by fluctuations in river stage and can vary considerably [6].

Persistent losing conditions in a river–alluvial aquifer system favor a transitional state between hydraulic connection and disconnection. As explained by [1] in consideration of a gaining perennial segment of river reversing into a losing segment and entering into a transitional state between hydraulic connection and disconnection, an increase in the depth to the phreatic surface beneath the river will decrease the rate of GW flow into the river until the heads in the aquifer and river are equal and no gain or loss occurs. Further increases in the depth to the phreatic surface will result in the river losing SW into the aquifer until the phreatic surface is sufficiently deep relative to the riverbed to develop

an unsaturated zone between the river and aquifer. When an unsaturated zone exists between the river and aquifer, the infiltration rate of the SW into the aquifer asymptotically achieves a constant value [1] where further reductions in the depth to the phreatic surface no longer influence the infiltration rate, and the river is said to be hydraulically disconnected from the alluvial aquifer [1]. The basic requirements for disconnection are the presence of a low-hydraulic-conductivity layer beneath the riverbed and a capillary fringe above the phreatic surface that does not intersect the base of the low-conductivity layer [1]. In a disconnected river–alluvial aquifer system, changes in the depth to the phreatic surface in the alluvial aquifer do not affect the infiltration rate of the SW into the low-conductivity layer between the riverbed and the unsaturated zone in the alluvial aquifer [1]. Additional declines in the GW table elevation near the riverbed will result in a maximum infiltration flux from the river to the aquifer that is limited only by the hydraulic conductivity of the low-permeability layer and the river stage [6].

Despite the large number of scientific studies on SW-GW exchanges in perennial rivers available in the literature, knowledge gaps still remain with respect to hydraulic connectivity and transitions between different states of intermittent connection in ephemeral rivers, even though they are some of the most common and dynamic hydrologic systems that occur on every continent [11,14,15]. Addressing the knowledge gaps requires the development of new methods of monitoring the spatial and temporal changes in states of hydraulic connection between rivers and alluvial aquifers and gaining and losing conditions in hydraulically connected river–alluvial aquifer systems over the range of spatial and temporal scales under which they vary. Electrical geophysical methods have a key role to play in this endeavor because the electric potential field created by streamflow over porous geologic sediments changes amplitude and polarity in direct response to changes in SW-GW exchange directions and rates, and the electrical properties of the alluvial aquifer sediments vary in direct response to changes in the saturation, temperature, and salinity of the GW [16].

Time-lapse self-potential (SP) monitoring and time-lapse electric resistivity tomography (ERT) surveys provide a means of studying the transient changes in hydraulic connectivity between ephemeral rivers and alluvial aquifers through the spatial and temporal changes in the electric potential field in the river and the electric resistivity of the riverbed and aquifer sediments. Time-lapse SP monitoring refers to continuous passive measurements of voltage differences between two or more electrodes in an electrode array that is oriented in either a profile or grid geometry and installed either on or beneath the riverbed, or alternatively, by floating the array above the riverbed in the SW. The transient changes of the measured voltage differences and the corresponding electric potential field that are detected by the electrodes in the array are caused by GW flow and advection of electrically charged ions through the porous riverbed sediments in addition to other natural sources of electric current in the subsurface including chemical diffusion along concentration gradients, thermoelectric effects attributed to heat conduction along temperature gradients, reduction–oxidation (redox) gradients, and biogeochemical reactions [17]. As a result, time-lapse SP monitoring has been used extensively in geophysical and hydrologic studies for purposes including but not limited to relating transient SP signals to hydrogeological and meteorological data and topographic effects [18]; studying long-term electrode drifts and stability characteristics [19,20]; studying diurnal electrical signals attributed to spring discharge, capillary fluxes, and surface temperature variability [21,22]; quantifying variations in sap flow in a tree trunk [23]; observing GW-level drawdown and recovery during aquifer tests [24]; mapping preferential GW flow paths by monitoring salt plume migration and thermal conduction and advection [25,26]; detecting GW flow in the vadose zone attributed to precipitation infiltration and vegetative transpiration [27]; monitoring redox conditions at the water table [28]; and monitoring depth profile variations of soil moisture, organic matter, and relative rates of microbial activity [29].

The geometry and polarity of the electric potential field in the river and adjacent flood plain depend upon the spatial and transient changes of the electric resistivity distribution

beneath the riverbed, which is mapped by time-lapse ERT [30]. Time-lapse ERT relies on the repeated creation and measurement of an artificial electric field at the land surface or in the riverbed through time. The artificial electric field is created by the active injection of an electric current into the subsurface and superimposed upon the natural electric field that is sensed by the SP electrode array. Each two-dimensional tomogram measured at a given moment in time is measured by sequencing subsets of four-electrode quadrupole arrays of the full ERT array, where two electrodes are designated as a current dipole and used to inject and extract electric current into the riverbed and two electrodes are designated as a potential dipole and used to measure the artificial electric potential field created by the current electrodes [30]. The resistance across the potential electrodes is measured for all sequenced combinations of quadrupole arrays in the ERT array and subsequently mapped to an apparent resistivity pseudo-section, which is inverse-modeled to produce a tomogram showing the approximate 2D electric resistivity distribution beneath the ERT array at a given moment in time. Transient changes in the resistivity of the riverbed sediments are attributed to changes in the mineralogy of the riverbed sediments and the saturation, porosity, and temperature of the riverbed and alluvium beneath the riverbed, in addition to changes in the salinity of the SW in the river and GW in the alluvial aquifer. Time-lapse ERT is therefore applicable in fluvial settings to monitor the way these properties of the riverbed, flood plain, and alluvial aquifer sediments change through time, and the resistivity data are required to make quantitative interpretations of the natural electric potential field that is measured during SP monitoring. Recent examples of applications of time-lapse ERT include studies aimed at monitoring vadose zone infiltration [31,32], permafrost dynamics in alpine terrain [33,34], internal erosion in embankment dams [35,36], leakage from underground storage tanks [37], salt transport along preferential flow paths [38], and DNAPL remediation efforts in a contaminated aquifer [39]. Additionally, ERT has been used extensively to study SW and GW exchanges between rivers and alluvial aquifers and for studying intermittency in hydraulic connections [11,40–51].

This paper describes the results of a geoelectric monitoring survey combining time-lapse SP and ERT to study SW-GW exchanges and transient intermittency of the hydraulic connection between the lower Rio Grande and the Rio Grande alluvial aquifer by measuring changes in the electric potential field in the riverbed and the electric resistivity of the alluvial aquifer sediments through time. The geoelectric monitoring survey was administered by the U.S. Geological Survey (USGS) in collaboration with New Mexico State University (NMSU), Elephant Butte Irrigation District (EBID), and hydroGEOPHYSICS, Inc (HGI) (Tucson, AZ, USA). Self-potential and ERT monitoring arrays were installed across a dry lower Rio Grande riverbed from 15 to 20 May 2022 to monitor voltage differences, electric potential, and changes in electric resistivity beneath the riverbed between 21 May 2022 and 4 October 2022 as streamflow conditions in the channel transitioned from completely dry to bank-full flow conditions during the irrigation season and back to dry conditions again after reservoir releases from dams in upstream basins were discontinued. The data and discussion herein seek to address one of the fundamental questions posed by [3] using the lower Rio Grande as a proxy for general inferences in other ephemeral rivers in arid and semi-arid environments: what are the effects of intermittent streamflow on the hydraulic connectivity between ephemeral rivers and alluvial aquifers? Focusing on this fundamental question, a methodology was developed for monitoring SW-GW exchanges and transient hydraulic connectivity between rivers and alluvial aquifers. Additionally, a suite of data-processing and analysis tools was developed to partition the SP monitoring data into component contributions from multiple naturally occurring sources (e.g., GW flow, chemical diffusion, and heat conduction). This work elucidates one of many foreseeable applications of the depicted geoelectric monitoring and data-processing approaches for enhanced hydrologic characterization of rivers.

2. Hydrogeology of the Mesilla Basin

The hydrogeology of the Mesilla Basin of southeastern New Mexico and southwestern Texas is summarized here from [52,53] and references cited therein. The Mesilla Basin aquifer system is the U.S. part of the Mesilla Basin (U.S.)/Conejos-Médanos (Mexico) aquifer system (Figure 1). The Mesilla Basin aquifer system (hereinafter referred to as the "Mesilla Basin aquifer") is hydraulically connected to the Conejos-Médanos aquifer system in Chihuahua, Mexico, and there are no natural barriers to inhibit groundwater flow across the border. In the Mesilla Basin, the Mesilla Basin aquifer is divided into two distinct hydrogeologic units, which are (from younger to older) the middle-to-late Quaternary (Holocene) channel and flood plain deposits of the Rio Grande alluvial aquifer (referred to herein as the "alluvial aquifer") and the poorly consolidated middle-Miocene to late-Pleistocene basin-fill deposits of the Santa Fe Group aquifer system (hereinafter referred to as the Santa Fe Group).

The lower Rio Grande has deposited a 24–46 m thick surface layer of alluvial sediments through channel avulsion and overbank deposition. These sediments contain the alluvial aquifer and are hydraulically connected to the unconsolidated-to-semi-consolidated basin-fill deposits of the Santa Fe Group, which is between 610 and 914 m thick in the Mesilla Basin [52]. The alluvial aquifer is heavily relied upon in the Mesilla Basin for irrigation water and as a primary source of municipal and domestic water supply for numerous communities along the United States–Mexico border including Las Cruces, New Mexico (N. Mex.), El Paso, (Tex.), and Ciudad Juárez, Mexico [52,53]. The shallow alluvial aquifer receives recharge from the lower Rio Grande, but only about 11% of the withdrawn GW volume is recharged back to the alluvial aquifer annually—an amount that is less than recent withdrawals [54]. Alluvial GW geochemistry is governed by the evaporative concentration of salts, whereas deeper GW geochemistry is governed by mixing and geochemical processes [52,54,55].

The lower Rio Grande is ephemeral in the Mesilla Basin and flows from north to south for short discontinuous periods. The river is dry most of the year, except during the irrigation season when streamflow is provided by reservoir releases from dams in upstream basins [52,54] and to a lesser degree following extreme precipitation events. The hydraulic connectivity between the lower Rio Grande and the alluvial aquifer varies spatially and temporally when streamflow is conveyed [11]. During the irrigation season when streamflow is conveyed, the river can be hydraulically connected to the alluvial aquifer at one location while simultaneously disconnected from the alluvial aquifer at a different location, and the state of hydraulic connection has been shown to be reversible when GW is withdrawn from the alluvial aquifer [3]. The river alternates between gaining and losing conditions in the Mesilla Basin, and water quality generally degrades in a downstream direction with chloride concentrations more than doubling between the inlet and the outlet of the basin [55,56]. Increases in salinity of the SW in the lower Rio Grande are attributed to runoff and recharge from agricultural activity, wastewater discharge into the river, the evaporative concentration of salts, topographic and buoyancy-driven upwelling of geothermal GW and non-thermal saline GW [55,56], and intra-basin GW flow from surrounding basins [56].

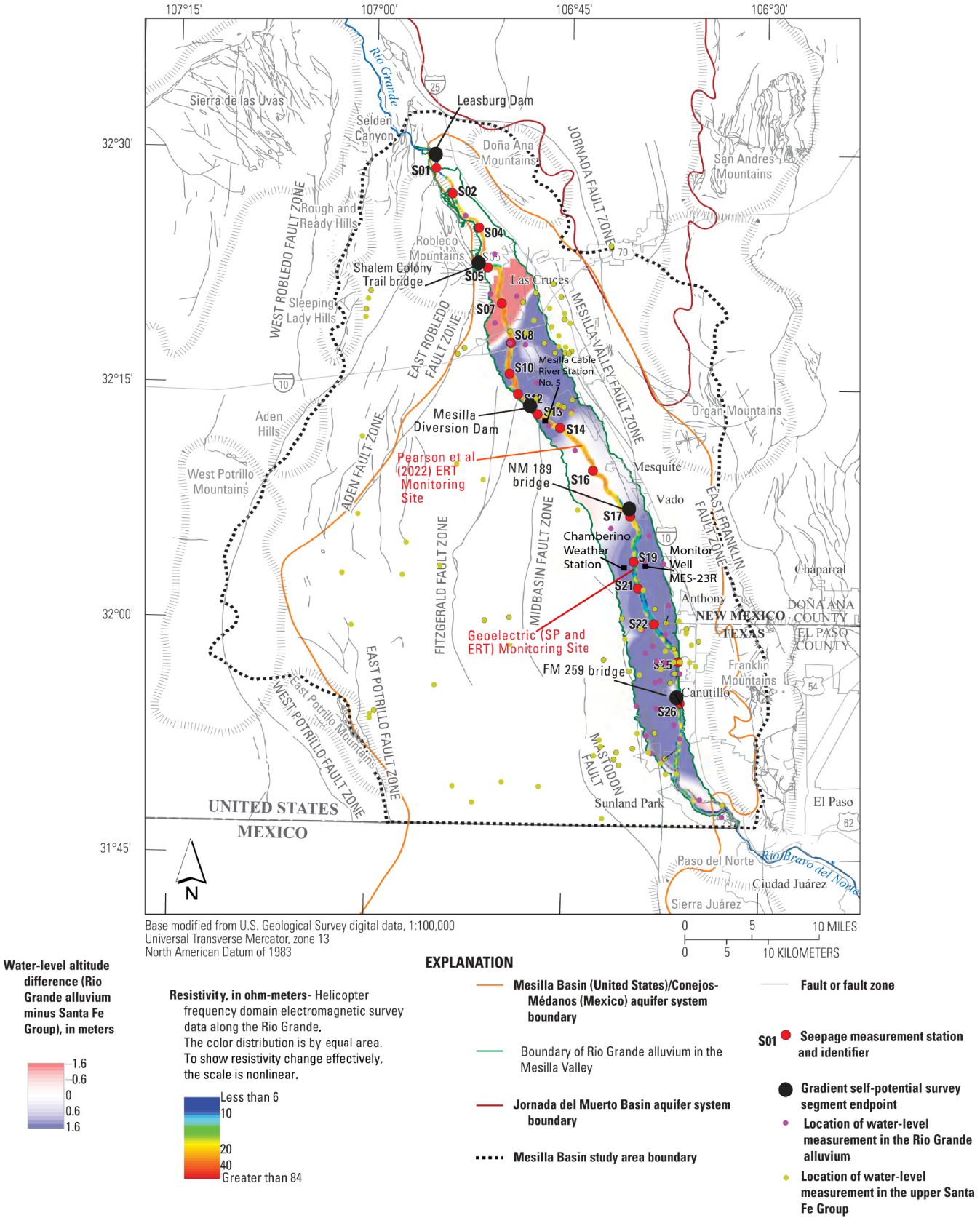

Figure 1. Location map of the Mesilla Basin showing geospatial relations between relevant hydrologic and geophysical datasets. The location map was reproduced with permission from *Water* (Figure 3 in [53]). The location of the geoelectric monitoring site is shown between seepage stations S19 and S21 (red dots) relative to the location of the monitoring site studied by [11].

2.1. Summary of Previous Geophysical and Hydrologic Surveys in the Mesilla Basin

The lower Rio Grande has been studied extensively in the Mesilla Valley by geophysical, geochemical, and hydrologic surveys. Annual seepage investigations were conducted by [57] during 2006–2013 along a 103-kilometer (km)-long segment of the lower Rio Grande in the Mesilla Valley, beginning just downstream from Leasburg Dam, N. Mex., and ending downstream from Canutillo, Tex. (Figure 1). During 2006–2013, seepage losses were measured at the same locations where the USGS measured seepage losses annually from 1988 to 1998 and from 2004 to 2013 [57]. Annual seepage investigations were completed each year during 2006–2013 over 1–2 days each February during low-flow conditions, and discrete discharge measurements were made at 26 locations [57], 17 of which were on the main stem and are shown in Figure 1 (red dots, S01–S26). Median values of the seepage data from [57] were calculated and summarized by [52] and are represented by the blue dots in Figure 2. The median values of the [57] seepage data indicated that for the 1–2 days of each February that were studied, the lower Rio Grande was generally a losing stream between Leasburg Dam and Mesilla Diversion Dam, and it had some losing and some gaining segments downstream from Mesilla Diversion Dam.

An extensive analysis of the geophysical, geochemical, and hydraulic characteristics of the GW flow system of the U.S. part of the Mesilla Basin aquifer is provided by [52]. For example, ref. [52] published maps of 2010–11 GW-level differences between the GW levels in the alluvial aquifer and the Santa Fe Group, in addition to horizontal and vertical hydraulic gradient maps beneath the Rio Grande riverbed in the Mesilla Valley. Figure 1 [52,53] (see also Figure 2) shows differences between 2010–11 GW levels in the alluvial aquifer (measurement locations shown by pink dots) and the Santa Fe Group (measurement locations shown by yellow dots) in addition to the resistivity at a depth of 30.5 m below the riverbed. The 2010–11 GW-level differences between the alluvial aquifer and the Santa Fe Group show that the vertical hydraulic gradient in the lower Rio Grande varies substantially across the Mesilla Valley. GW-level elevations in the alluvial aquifer were generally higher than the GW-level elevations in the Santa Fe Group throughout most of the Mesilla Valley, corresponding to blue-shaded sections in Figures 1 and 2 (e.g., S08–S14 and downstream from S17). Blue-shaded sections indicate that GW-level differences were greater than 0 m, and the vertical hydraulic gradient was predominantly oriented downward such that SW losses were likely to occur. Reductions and reversals of the vertical hydraulic gradient were also indicated by the 2010–11 water-level differences mapped in Figure 1 by the white sections (e.g., S14–S17) and red sections (e.g., S05–S08), respectively. In these locations, the vertical hydraulic gradient either decreased substantially or flattened across faults that intersected the channel or reversed direction, resulting in SW gains.

The color shading of the GW-level differences in Figure 1 is also indicated in Figure 2 and compared to the seepage data of [57] and the electric resistivity of the riverbed and alluvial aquifer sediments at depths of 3.5 m and 50 m beneath the land surface. The electric resistivity profiles in Figures 1 and 2 show that notable resistivity contrasts occur longitudinally in the direction of SW flow between seepage stations S01 and S26, as well as vertically in the first 50 m beneath the riverbed. A noticeable longitudinal change in resistivity occurs just downstream from seepage station S17 (Figure 1), where resistivity at 30.5 m beneath the riverbed changes from relatively higher resistivity values of 20 ohm-m and greater to relatively lower resistivity values of less than or equal to about 10 ohm-m. The resistivity profiles in Figure 2b show notable reductions in resistivity vertically between 3.5 and 50 m beneath the riverbed, particularly in white and blue-shaded sections downstream from Mesilla Diversion Dam between seepage stations S13 and S14. Notable resistivity transitions were observed by [52] near Vado, New Mex., between depths of 3.5 and 50 m beneath the land surface where the resistivity values changed from relatively high resistivity values greater than 20 ohm-m to relatively low resistivity values less than 10 ohm-m (Figure 2b at distances greater than about 32 km).

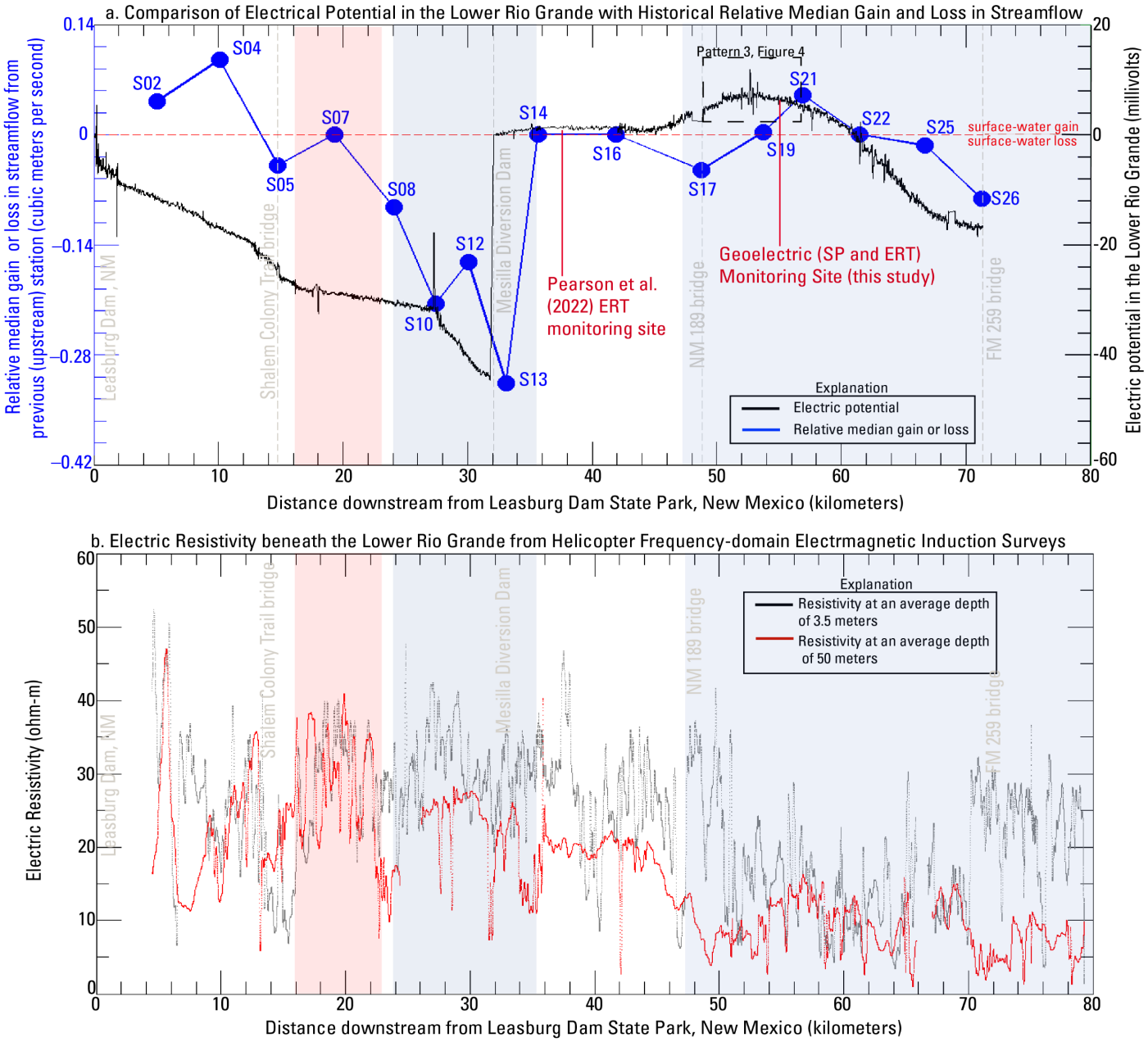

Figure 2. Waterborne self-potential and electric resistivity at depths of 3.5 m and 50 m beneath the Rio Grande riverbed, and relative median streamflow gain or loss along a 72 km long segment across the Mesilla Valley, reproduced with permission from *Water* (Figure 9 in [53]). (**a**) Comparison of profiles of relative median streamflow gain and loss [57] (blue, left vertical axis) with electric potential [53] (black, right vertical axis) measured in the Rio Grande. (**b**) Electric resistivity [52] at average depths of 3.5 m and 50 m beneath the riverbed from helicopter frequency-domain electromagnetic sounding. Color shading represents the water-level altitude differences depicted in Figure 1. The location of the geoelectric monitoring site for this study is indicated relative to the location of the ERT monitoring site studied by [11].

In addition to GW-level elevation difference and vertical hydraulic gradient maps, [52] published a three-dimensional resistivity model in the southern part of the Mesilla Basin near Paso del Norte. The resistivity model was developed by kriging inverted resistivity from a compilation of historical resistivity datasets obtained from helicopter frequency-domain electromagnetic induction surveying of the Rio Grande levee system [58], ground-based time-domain electromagnetic induction soundings [52], and vertical electrical soundings completed within the Mesilla Basin by [59] and presented by [52] as a

series of gridded resistivity depth slices between depths of 0 m (at or about the land surface) and 570 m beneath the land surface (an interactive PDF file of the model is available from [52]). Four of the resistivity depth slices are shown in Figure 3, corresponding to depths of 0, 152, 305, and 457 m below the land surface in the southern Mesilla Basin. Near the land surface (that is, at or about 0 m below the land surface), the depth slices show resistivity values that are generally greater than 20 ohm-m and are consistent with the resistivity profiles shown in Figure 2b. Slightly more than 25 percent of the gridded resistivity values in the 3D model were relatively low and less than or equal to 10 ohm-m. With increasing depth, resistivity values less than 10 ohm-m are more prevalent; about half of the resistivity values were less than 10 ohm-m at depths greater than 50 m, and at progressive depths of 152 m, 305 m, and 457 m, low resistivity values become progressively more widespread, as shown in Figure 3.

An upwelling saline plume of GW, upwelling at a depth within the Mesilla Basin aquifer through fractures within the basin bedrock, was interpreted by [52] through a comparison of gridded resistivities with a large dataset of total dissolved solids concentrations of GW samples acquired in wells completed within the Santa Fe Group between 1922 and 2007. The resistivity values correlated to TDS were obtained from the 3D resistivity model at the same depths the TDS samples were collected in the field. Total dissolved solids concentrations of more than 1000 mg/L were common in the southern part of the Mesilla Basin where low resistivity values were widely present in the subsurface, especially with increasing depth. Some of the dissolved solids concentrations were greater than 3000 mg/L, and in general, the distribution of TDS concentrations represented conditions ranging between moderately saline and very saline GW. The comparison between the dissolved solids concentrations and the resistivity data indicated a good correlation between low resistivity values and high dissolved solids concentrations. Higher dissolved solids concentrations were generally associated with lower resistivity values (less than or equal to 10 ohm-m), and lower dissolved solids concentrations were generally associated with higher resistivity values (greater than 10 ohm-m).

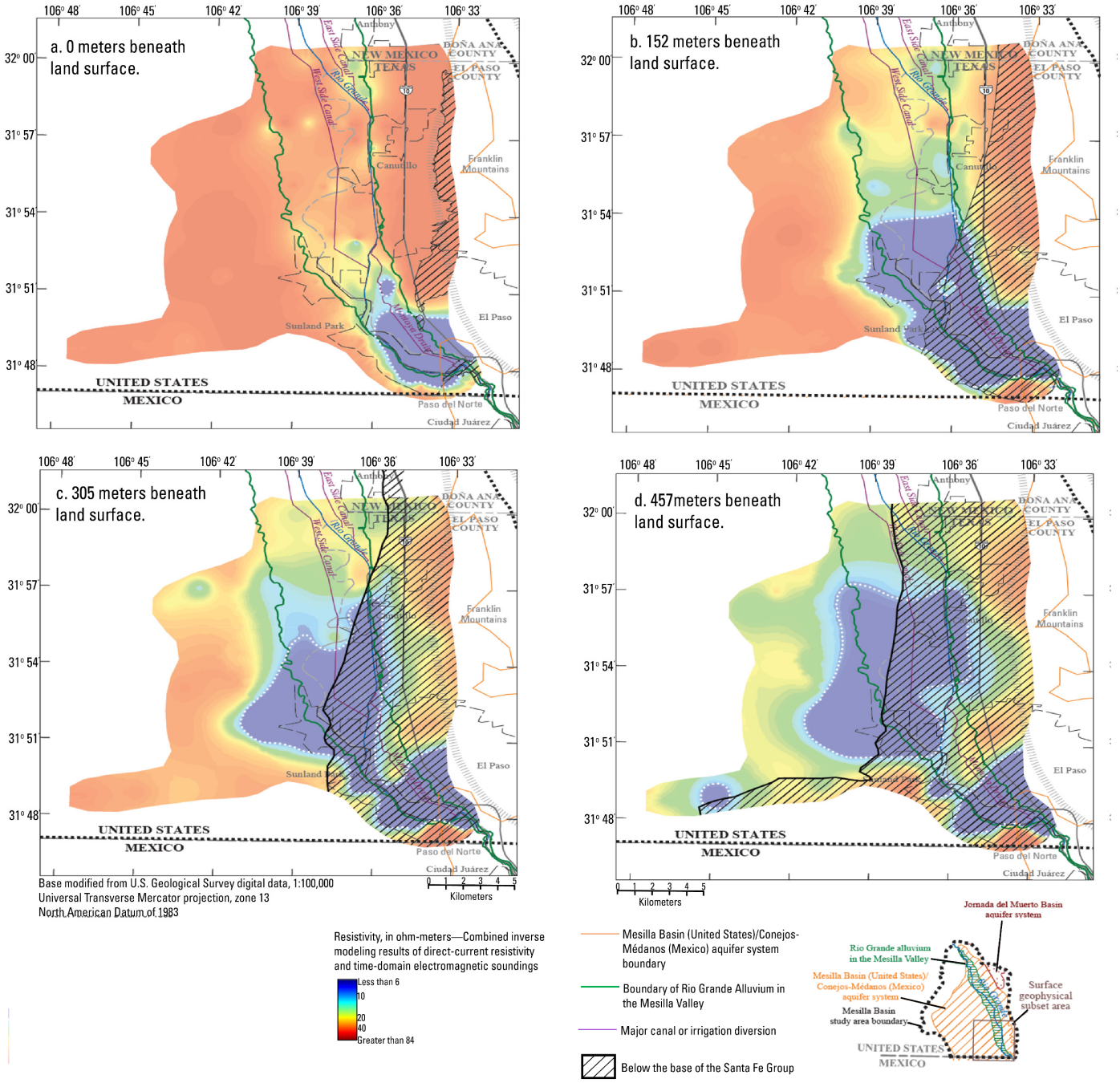

Figure 3. Gridded resistivity values from the combined inverse modeling results of the direct-current resistivity and time-domain electromagnetic soundings at depths of (**a**) 0 m; (**b**) 152 m; (**c**) 305 m; and (**d**) 457 m below land surface in the Mesilla Basin south of the study area. Reproduced from [52]; used with permission.

A waterborne SP logging survey of the lower Rio Grande in the Mesilla Basin was completed by [53] from June to July 2020 to map gaining and losing segments of the river by measuring the electric potential field in the river. This 2020 survey produced 72 km long profiles of SW temperature, SW specific conductance, and electric potential measured from a floating kayak, which were interpreted by [53] as qualitative geophysical indicators of SW gain and loss in the lower Rio Grande throughout the Mesilla Valley. The electric potential profile data measured by [53] are shown by the black data in Figure 2a and resemble the relative median gain/loss curve (Figure 2a; blue data) processed from the [57] seepage data by [52]. The corresponding SW temperature and SW conductivity

measurements acquired along the 72 km long survey segment of [53] are represented in Figure 4 as deviations in the temperature and specific conductance relative to the initial values at the upstream end of the surveyed segment. The temperature and specific conductance data logged along segment 4 of the [53] SP survey segment are shown by the blue data and correspond to the location of the monitoring site described in Section 2.2. These data display two distinct relations between temperature and specific conductance along segment 4. Pattern 3, corresponding to the segment between seepage stations S17 and S21, shows lower SW temperature deviations corresponding to higher specific conductance deviations, whereas the other apparent relation (pattern 4) shows lower specific conductance deviations corresponding to higher SW temperature deviations.

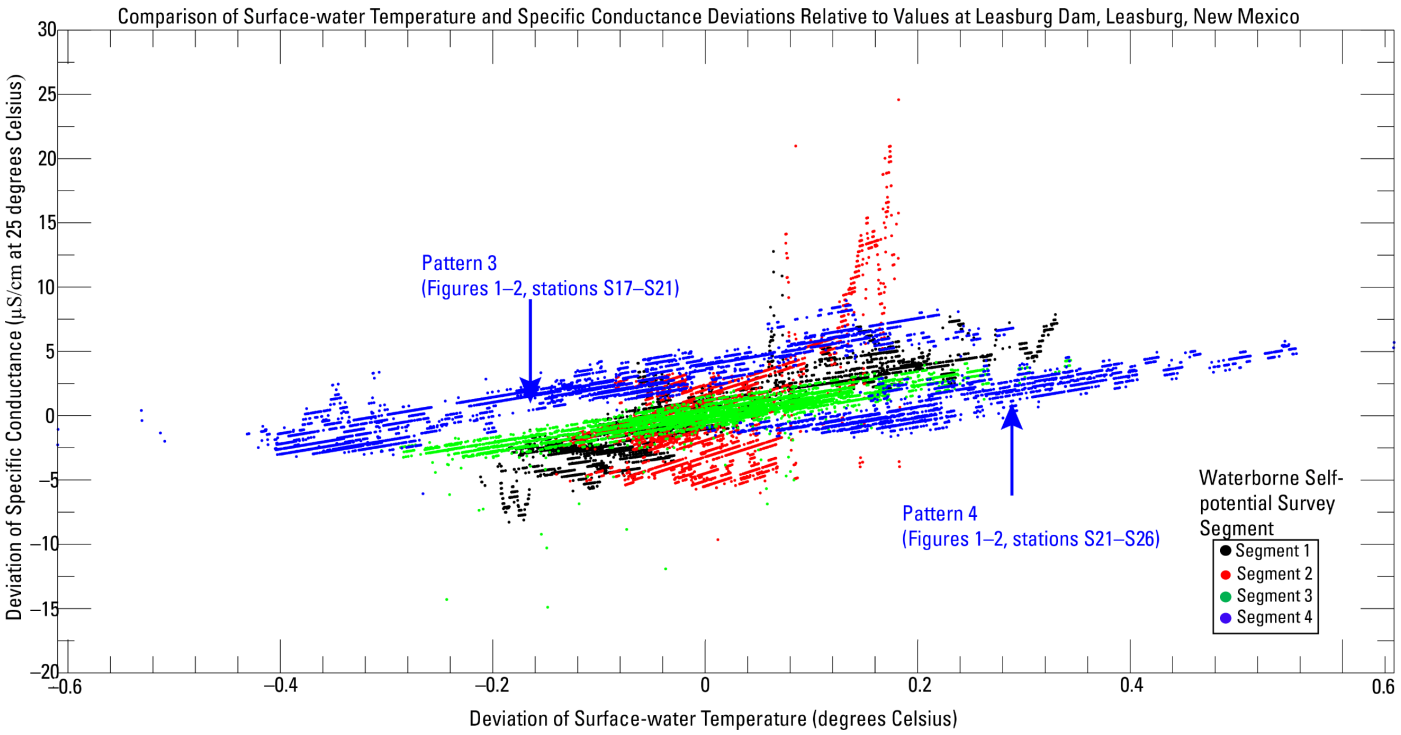

Figure 4. Scatterplot of deviations in SW specific conductance and SW temperature, relative to the values at the upstream end of the segment measured during a waterborne SP logging survey of the Rio Grande across the Mesilla Valley. Reproduced with permission from *Water* (Figure 10 in [53]). Segment 1: Leasburg Dam to Shalem Colony Trail bridge; segment 2: Shalem Colony Trail bridge to Mesilla Diversion Dam; segment 3: Mesilla Diversion Dam to New Mexico Highway 189 bridge; and segment 4: New Mexico Highway 189 bridge to Farm to Market 259 bridge Canutillo, Tex.

Pearson et al. [11] studied a cross-section of an ephemeral segment of the lower Rio Grande in Mesquite, New Mexico, downstream from the Mesilla Diversion Dam where the [57] seepage data (Figure 2a; blue) and [53] electric potential data (Figure 2a; black) indicated that static to slight gaining conditions could exist. Their monitoring approach used time-lapse electrical resistivity tomography to characterize the spatiotemporal connectivity of the river with the GW level in the alluvial aquifer for a period of 1 year including the 2020 irrigation season. They monitored transient changes in connectivity between the SW in the river and GW in the alluvial aquifer from hydraulically disconnected conditions to connected conditions and back to disconnected conditions again, which occurred before, during, and after periods of streamflow, respectively. In conjunction with a large supporting dataset that consisted of time-series of flood plain GW levels, streamflow, river stage, SW and GW temperature, and electric conductivity measurements, ref. [11] demonstrated that SW and GW temperatures were the main drivers of the time-lapse changes that they observed in the electric resistivity of the riverbed. Their ERT monitoring approach indicated that the hydraulic connection between SW and GW occurred rapidly

upon the arrival of streamflow at their monitoring site. The ERT monitoring study performed by [11] outlines the framework for geoelectric monitoring described herein using time-lapse SP monitoring and time-lapse ERT.

2.2. Description of the Geoelectric Monitoring Site

The geoelectric monitoring site is located at coordinates (32.0628 N, 106.6635 W) (World Geodetic System 1984 [WGS84] datum) between Vado, N. Mex., and Anthony, N. Mex., about 23 river-km downstream from the Mesilla Diversion Dam in Mesilla, N. Mex., and downstream from the monitoring site studied by [11] in Mesquite, New Mex. (Figure 2). The location is annotated in Figures 1 and 2 between seepage stations S19 and S21 and is approximately 300 m downstream from the New Mex. Highway 226 bridge (West Berino Road) that crosses the river. This segment of the lower Rio Grande is ephemeral but shown as a general gaining segment by the [57] seepage data published by [52,57] (Figure 2a; blue curve) and the waterborne SP data published by [53] (Figure 2a; black curve), which both show general gaining conditions between stations S17 and S21. In contrast, the shaded GW-level differences in Figures 1 and 2 indicate that the Rio Grande at the geoelectric monitoring site may at times lose water to the underlying alluvial aquifer.

Streamflow at the monitoring site is controlled by releases of impounded SW from Elephant Butte Dam, Caballo Dam, and Mesilla Diversion Dam, all of which are upstream from the site. Streamflow during 2022 only occurred at the monitoring site during the irrigation season (4 June–21 August 2022), and to a lesser extent after extreme precipitation events, and the river and alluvial aquifer were hydraulically disconnected for the remainder of the year because there was no base flow supplied to the river from the alluvial aquifer [11]. However, during the irrigation season, a nearly constant river stage is maintained for a sustained period of time by planned SW releases, allowing a hydraulic connection between the river and alluvial aquifer to develop [11].

3. Materials and Methods

The general layouts of the SP and ERT monitoring arrays are depicted in Figure 5. Two trenches were excavated in the medium-fine and fine-sand sediments of the west flood plain and riverbed with a mini excavator. The SP and ERT electrode arrays were installed into the flood plain and riverbed in the SP and ERT trenches, respectively. Figure 5a shows a photograph of the backfilled SP trench about 13 m upstream from the instrumented ERT trench. The SP electrode array consisted of 30 non-polarizing copper-sulfate electrodes, each buried approximately 1.2 m beneath the riverbed at the bottom of the trench, encased in bentonite clay to reduce contact resistance between the electrodes and dry riverbed sediments, and offset laterally from adjacent electrodes in the array by a distance of 3 m on average, as shown by the plan-view site map in Figure 5b. SP electrodes 1–10 were installed on the west flood plain, whereas SP electrodes 11–30 were installed into the riverbed beginning at the base of the west bank and spanning 55–60 m across the riverbed to the base of the east riverbank. Electrodes were not installed in the west bank to avoid excavating beneath the tree that housed the data logging instrumentation. Electrodes were not installed into the east bank or flood plain because of the vegetation on the east bank. Each individual SP electrode is numbered and color-coded in Figure 5b,c for data display purposes, and the colors correspond to the plotted SP time-series and profile data in subsequent figures.

The ERT electrodes were installed into the riverbed about 13 m downstream from the SP array. The ERT electrode array consisted of 56 electrodes, each buried approximately 0.9–1.2 m beneath the riverbed and separated laterally from adjacent electrodes in the ERT array by a distance of about 1.3 m on average, as shown in the plan-view map in Figure 5b. ERT electrodes 1–12 were installed in the west flood plain and west bank, whereas the remainder of the ERT electrodes were installed directly into the riverbed between the base of the west bank and the base of the east bank. A vertical cross-section depicting the elevations of the SP electrodes relative to the elevations of the ERT electrodes and the

riverbed surface (black curve) is shown in Figure 5c. Elevations and horizontal coordinates of the SP and ERT electrodes shown in Figure 5c were measured by real-time kinematic global navigation satellite systems (GNSS) positioning using two Trimble R8 GPS receivers and are accurate to within about 2 cm horizontally and 5–6 cm vertically.

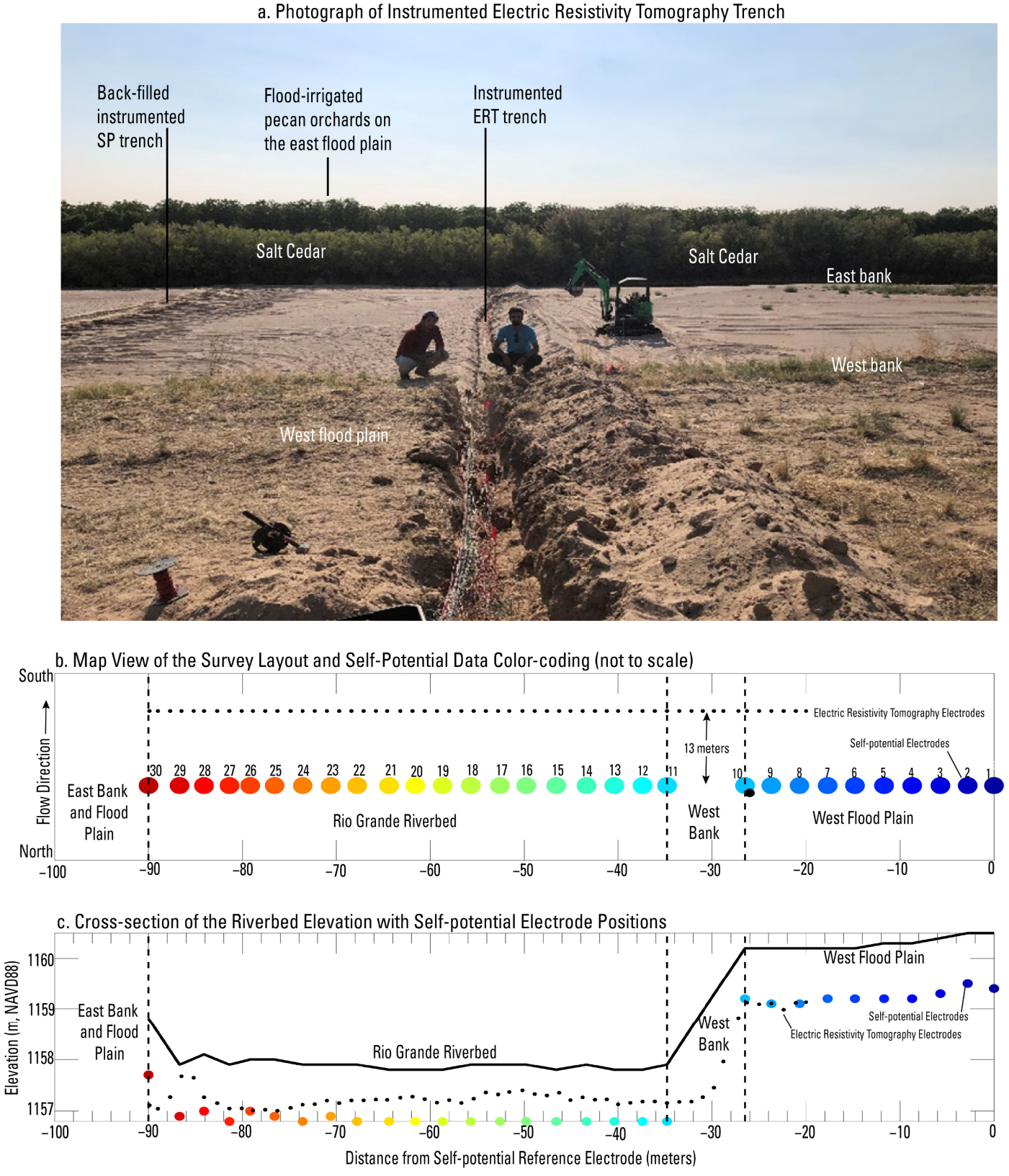

Figure 5. Overview of the geoelectric monitoring instrumentation and monitoring survey layout showing the data color-coding scheme for SP data and the spatial relations between the SP and ERT monitoring arrays including (**a**) photograph of the instrumented ERT trench (taken 18 May 2022, by Scott Ikard, U. S. Geological Survey, looking from the west flood plain towards the east bank); (**b**) map-view layout of the geoelectric monitoring site showing the locations, numbering, and data color-coding for SP electrodes used for plots of time-series data measured at each electrode; and (**c**) cross-section view of the geoelectric monitoring site showing the Rio Grande riverbed geometry and the vertical positioning of the SP and ERT electrodes.

3.1. Self-Potential Data Acquisition and Processing

SP monitoring data were measured at intervals of 60 s per measurement during the background and post-streamflow monitoring periods and 900 s per measurement during the streamflow monitoring period. SP monitoring data were not acquired during the short window of time corresponding to the streamflow arrival period because of a brief equipment malfunction that resulted in a loss of data, although time-lapse ERT data for multiple resistivity tomograms were acquired in rapid succession as streamflow arrived and infiltrated into the riverbed.

Figure 6 shows time-lapse voltage differences measured at each SP electrode during the 12-day-long background monitoring period between 07:59 a.m. Mountain Daylight Time (MDT) on 21 May and 2 June 2022. The background monitoring period data were acquired to develop a data-processing algorithm to apply to the data acquired during other monitoring periods and to provide a basis for analyzing electric potential variations during the other periods relative to the electric potential representative of the initial hydraulic condition of the background monitoring period. Figure 6a shows the raw voltage differences measured, each of which displays linear increases or decreases in electrode drift through time. Electrode drift corrections were applied to the raw voltage differences in Figure 6a by determining the electrode drift rate (the slope of the increasing or decreasing time-series voltage differences) for each color-coded time-series in Figure 6a as a function of the elapsed monitoring time and then calculating an electrode drift value at each measurement time and subtracting it from the raw voltage difference measured at the corresponding time. The electrode drift correction was applied to the raw voltage difference data using Equations (1) and (2), where ΔV_d (in millivolts (mV)) is the electrode drift voltage (the portion of the measured voltage difference that is attributed to electrode drift), $\Delta V/\Delta t$ (mV/s) is the electrode drift rate determined from the SP monitoring data measured prior to streamflow arrival, t (s) is the elapsed time since monitoring began, ΔV (mV) is the raw measured voltage differences shown in Figure 6a, and ΔV_c (mV) is the voltage differences corrected for electrode drift, shown in Figure 6b,c.

$$\Delta V_d = \frac{\Delta V}{\Delta t} t \quad (1)$$

$$\Delta V_c = \Delta V - \Delta V_d \quad (2)$$

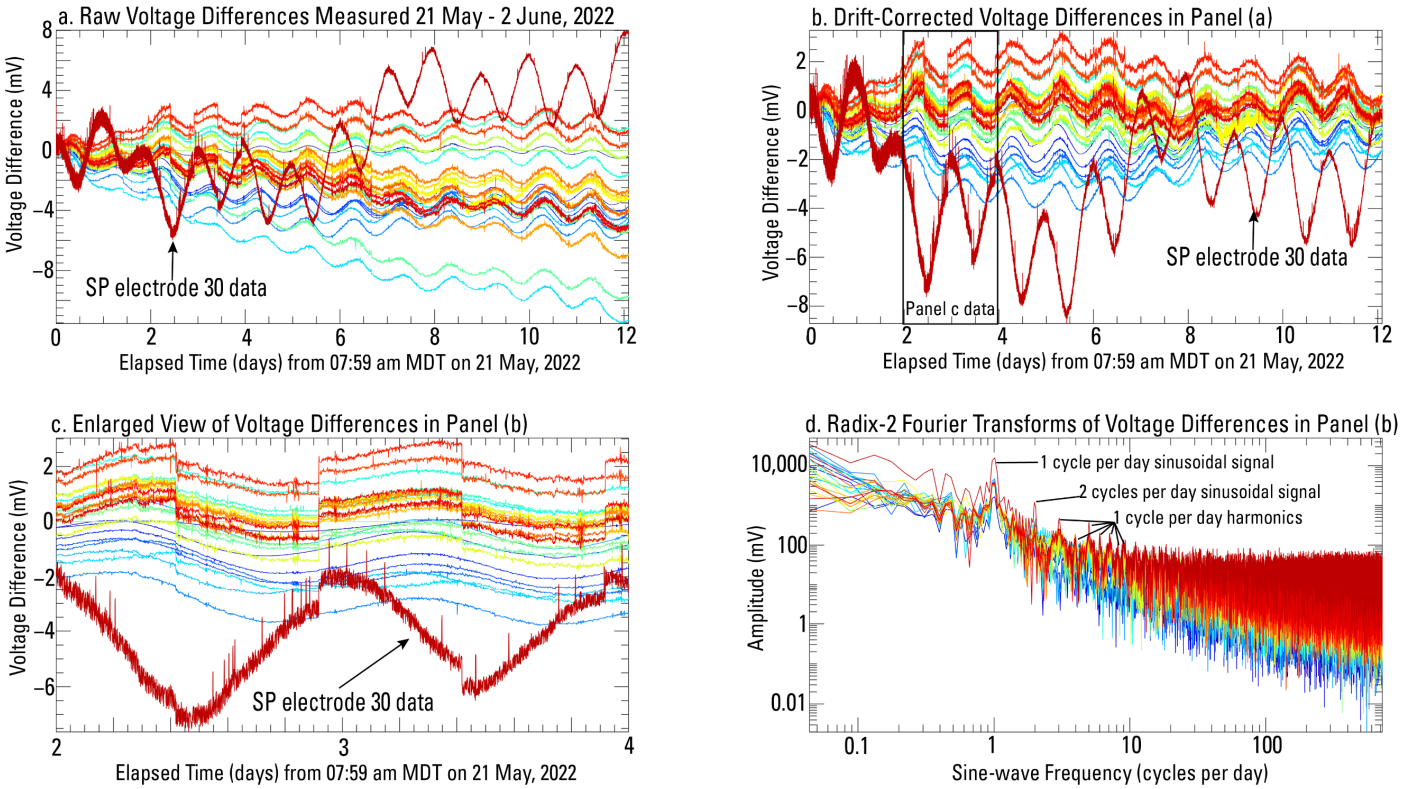

Figure 6. Illustration of the electrode drift corrections and frequency spectrums of voltage difference time-series measured at each electrode in the SP monitoring array between 07:59 a.m. Mountain Daylight Time on 21 May 2022 and 2 June 2022 corresponding to the background monitoring period. (**a**) Raw time-series of voltage differences measured at each electrode. (**b**) Drift-corrected time-series of voltage differences measured at each electrode. (**c**) Enhanced view of the black box in panel (**b**) showing the presence of a 1-cycle-per-day periodic fluctuation in the drift-corrected voltage difference time-series. (**d**) Frequency spectrums of drift-corrected voltage difference time-series (**b**) computed by discrete fast Fourier transform indicating the presence of the 1-cycle-per-day and 2-cycles-per-day signals and harmonics. Colors indicate the spatial position of the measured time-series in the SP electrode array, and correspond to numbered SP electrodes depicted in Figure 5.

Figure 6c shows an enlarged view of the drift-corrected voltage-difference data encapsulated by the black box in Figure 6b. The drift-corrected voltage differences show sinusoidal oscillation and discrete shifts in the time-series data corresponding to each electrode. The drift-corrected voltage differences in Figure 6b were therefore transformed to the frequency domain by computing the frequency spectrum by radix-2 fast Fourier transform using Equation (3), where $X(\omega)$ (mV) is the voltage difference time-series transformed into the frequency domain, $\omega = 2\pi T^{-1}$ is the angular frequency (radians/s) for measurement period T = 60 s per sample for pre- and post-streamflow monitoring data and 900 s per sample otherwise, $\Delta V_c[t]$ is the discrete sequence of drift-corrected voltage difference time-series at time index t = 1…N, e is the exponential function, and $j = \sqrt{-1}$ is the complex-valued variable.

$$X(\omega) = \sum_n \Delta V_c[t] e^{-j\omega t} \quad (3)$$

The frequency spectrums of the drift-corrected voltage differences are shown in Figure 6d. The transformed data indicate that the drift-corrected voltage-difference time-series data contained two sinusoidal signals—one with a diurnal frequency of 1 cycle per day and a larger amplitude that increases from the west flood plain towards the east bank of the river and a second sinusoid characterized by a 2-cycles-per-day frequency and smaller amplitude. Harmonics frequencies of the 1-cycle-per-day signal are also evident in Figure 6d (up to about 10 cycles per day). These sinusoidal signals were removed from

the drift-corrected voltage-difference data in Figure 6b by recursive application of a notch filter to the data measured at each SP electrode.

The progression of recursive notch filtering is depicted in Figure 7 using data corresponding to SP electrode 30 as an example given the anomalous behavior of the electrode 30 data relative to the other data. The electrode 30 data are shown in Figure 7a, and the corresponding Fourier transformed data are shown in Figure 7b, where the presence of the 1-cycle-per-day sinusoid is clearly indicated. The first application of the notch filter to the drift-corrected voltage differences produced the notch-filtered output data, ΔV_{N1} (mV), shown by the black curve in Figure 7c. The 1-cycle-per-day sinusoid, ΔV_1 (mV), filtered from the drift-corrected voltage differences by the notch-filtering process, is related to the drift-corrected voltage differences by Equation (4). The corresponding Fourier transform of the notch-filtered data in Figure 7c is shown in Figure 7d, where the presence of the 2-cycles-per-day sinusoid is indicated and the 1-cycle-per-day sinusoid is absent. The 2-cycles-per-day sinusoid was removed by applying the notch filter a second time to the notch-filtered data in Figure 7c to produce the data in Figure 7e (black curve), which are free of the influence of the 1-cycle-per-day and 2-cycles-per-day sinusoids as indicated by the corresponding Fourier transformed data shown in Figure 7f. The 2-cycles-per-day sinusoid, ΔV_2 (mV), filtered from the drift-corrected voltage differences by the second application of the notch filter, is related to the drift-corrected voltage differences by Equation (5), where ΔV_{N2} (mV) represents the notch-filtered data and ΔV_2 (mV) represents the 2-cycles-per-day sinusoid. The 1-cycle-per-day sinusoids extracted by the recursive notch-filtering process from data measured at each SP electrode are plotted in Figure 7g, and the underlying causative sources of the diurnal fluctuations are considered further in Section 4.5. The 2-cycles-per-day sinusoid is regarded as a likely result of variations in the electric potential field of Earth attributed to tidal effects and is not considered further because of insufficient data (e.g., no tilt meter or extensometer data, etc.) to make an objective analysis.

$$\Delta V_{N1} = \Delta V_c - \Delta V_1 \tag{4}$$

$$\Delta V_{N2} = \Delta V_{N1} - \Delta V_2 \tag{5}$$

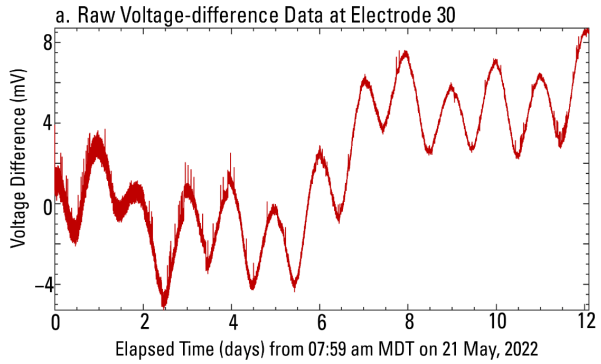
a. Raw Voltage-difference Data at Electrode 30
Voltage Difference (mV)
Elapsed Time (days) from 07:59 am MDT on 21 May, 2022

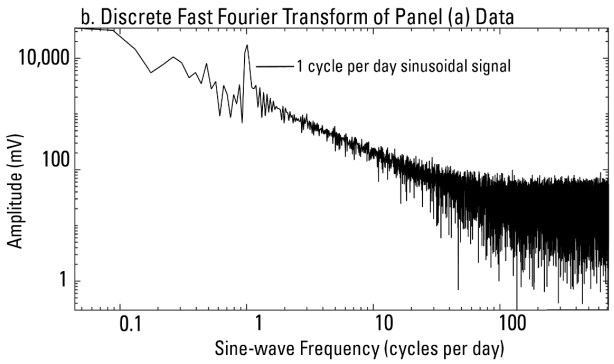
b. Discrete Fast Fourier Transform of Panel (a) Data
1 cycle per day sinusoidal signal
Amplitude (mV)
Sine-wave Frequency (cycles per day)

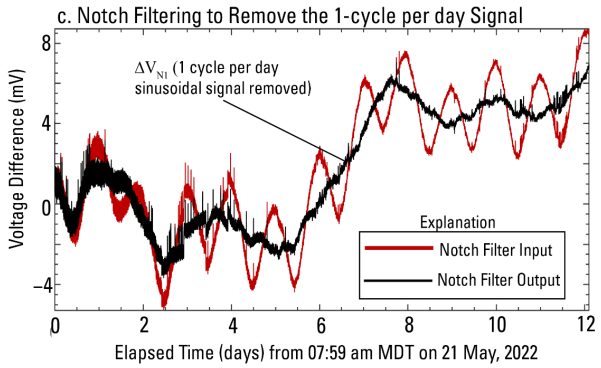
c. Notch Filtering to Remove the 1-cycle per day Signal
ΔV_N1 (1 cycle per day sinusoidal signal removed)
Explanation
Notch Filter Input
Notch Filter Output
Voltage Difference (mV)
Elapsed Time (days) from 07:59 am MDT on 21 May, 2022

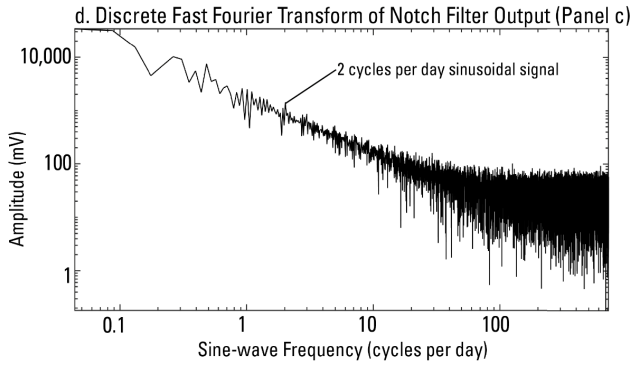
d. Discrete Fast Fourier Transform of Notch Filter Output (Panel c)
2 cycles per day sinusoidal signal
Amplitude (mV)
Sine-wave Frequency (cycles per day)

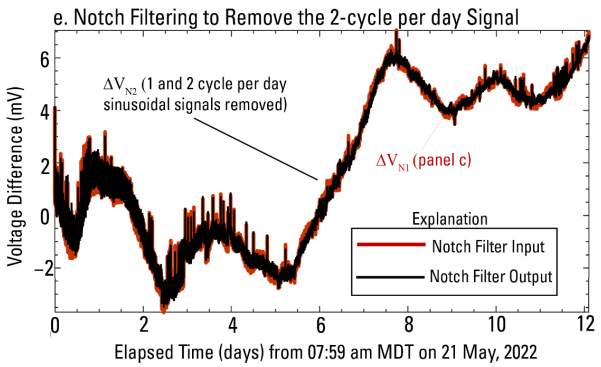
e. Notch Filtering to Remove the 2-cycle per day Signal
ΔV_N2 (1 and 2 cycle per day sinusoidal signals removed)
ΔV_N1 (panel c)
Explanation
Notch Filter Input
Notch Filter Output
Voltage Difference (mV)
Elapsed Time (days) from 07:59 am MDT on 21 May, 2022

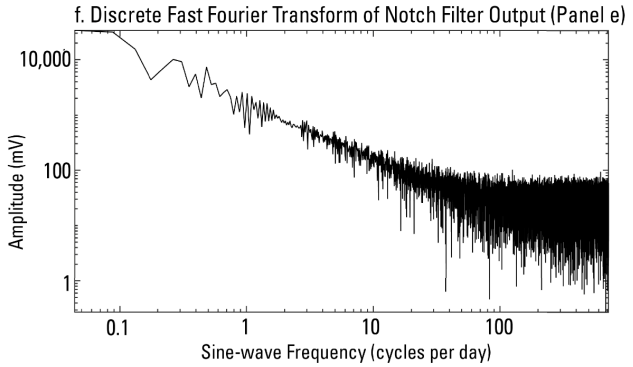
f. Discrete Fast Fourier Transform of Notch Filter Output (Panel e)
Amplitude (mV)
Sine-wave Frequency (cycles per day)

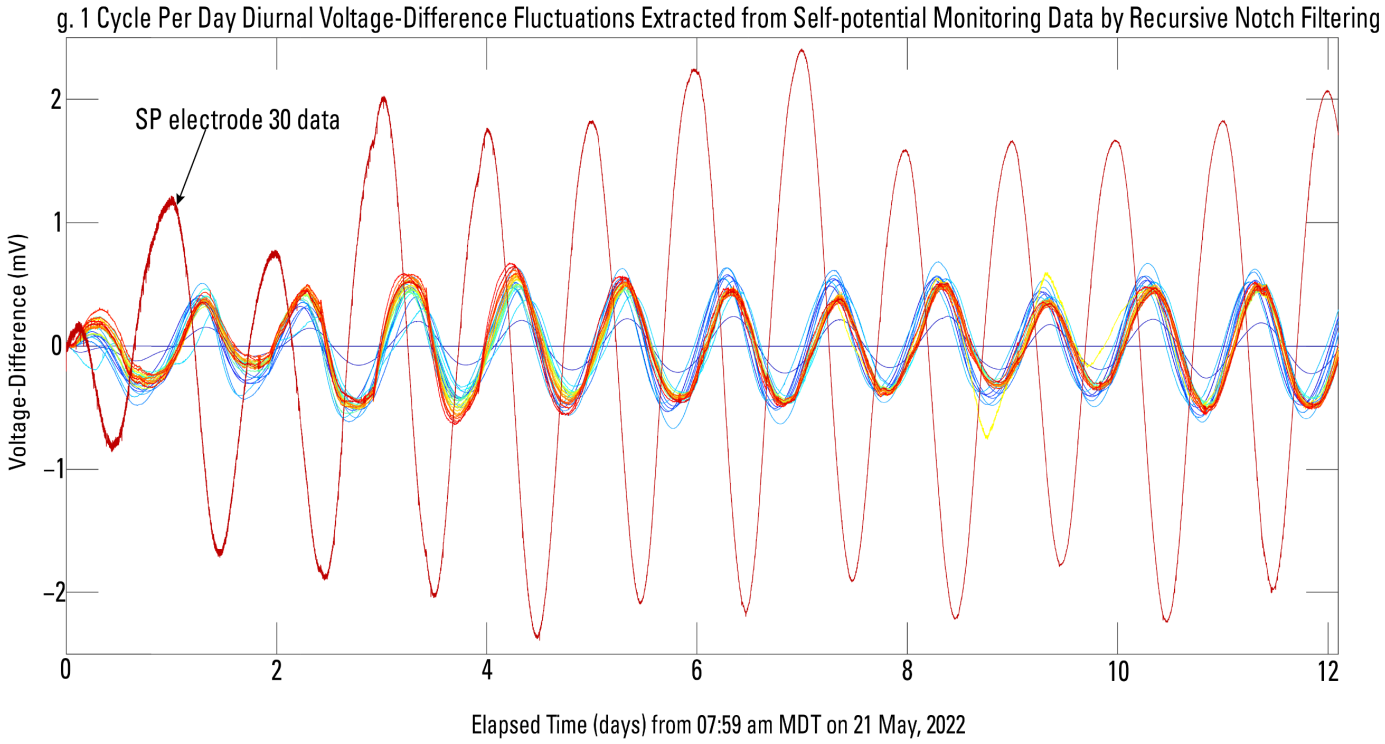
g. 1 Cycle Per Day Diurnal Voltage-Difference Fluctuations Extracted from Self-potential Monitoring Data by Recursive Notch Filtering
SP electrode 30 data
Voltage-Difference (mV)
Elapsed Time (days) from 07:59 am MDT on 21 May, 2022

Figure 7. Illustration of the notch filtering applied to drift-corrected voltage difference time-series data. (**a**) Drift corrected voltage difference time-series measured on electrode 30 during the background monitoring period. (**b**) Discrete fast Fourier transform of the data in panel (**a**) showing a large-amplitude 1-cycle-per-day periodic fluctuation in the data (**c**) Notch-filtered data (black) compared to pre-notch-filtered data (red) (**d**) Discrete fast Fourier transform of the black data in panel (**c**) showing that the 1-cycle-per-day periodic fluctuation has been removed and that the 2-cycles-per-day sinusoidal component is present. (**e**) Notch-filtered data (black) compared to pre-notch-filtered data (red). (**f**) Discrete fast Fourier transform of the black data in panel (**e**) showing that the 2-cycles-per-day periodic fluctuation has been removed. (**g**) Illustration of the one-cycle-per-day voltage difference time-series data extracted from the background monitoring period SP measurements by notch filtering. Colors indicate the spatial position of the measured time-series in the SP electrode array, and correspond to numbered SP electrodes depicted in Figure 5.

After making drift corrections and applying recursive notch filtering, the voltage difference time-series data were converted to time-series of electric field intensity by Equation (6), where $E_j[t]$ (mV/m) is the electric field intensity at electrode j at time index t, $\Delta V_j[t]$ (mV) is the drift-corrected, notch-filtered voltage difference measured between electrode j and electrode 1 at time index t, Δx_j (m) is the linear distance along the SP electrode array between electrode j and electrode 1, and j is an electrode index that ranges between values of 2 and 30.

$$E_j[t] = -\frac{\Delta V_j[t]}{\Delta x_j} \tag{6}$$

The time-series of electric field intensities calculated from Equation (6) were then numerically integrated into time-series of electric potential using Equation (7), where $V_j[t]$ (mV) is the electric potential at the electrode j at time index t.

$$V_j[t] = -V_j[t-2] - \tfrac{1}{3}E_j[t] + \tfrac{4}{3}E_j[t-1] - \tfrac{1}{3}E_j[t-2] \tag{7}$$

The processing sequence illustrated above, developed from the background monitoring period data measured prior to streamflow, was applied to the full SP monitoring time-series acquired between 21 May and 4 October 2022 to reference the time-series data during streamflow and post-streamflow monitoring periods to the background monitoring data so that changes from the background condition prior to streamflow could be analyzed after streamflow arrival at the monitoring site.

3.2. Electric Resistivity Tomography Data Acquisition and Processing

Self-potential monitoring data were not acquired during the streamflow arrival monitoring period; however, a SuperSting R8 electrical resistivity meter (Advanced Geosciences, Inc., Austin, TX, USA) was used to collect electrical resistance data along the two-dimensional cross-section of the ERT trench. Similar to the methods of [11], time-lapse tomographic measurements of resistance data and the corresponding apparent resistivity distributions beneath the ERT monitoring trench were acquired before, during, and after streamflow arrival at the monitoring site using the four-pole Alt-3 Wenner array [60]. The Alt-3 Wenner array measurements included the standard Wenner array measurements supplemented with gradient array measurements that were added to unused channels in the multichannel system to enhance the spatial resolution and increase the signal-to-noise ratio of the measured data [61]. ERT electrodes were connected to a breakout panel by wires that were run through the ERT trench (Figure 6a), and the breakout panel was connected to a multiplexor that was connected to the SuperSting R8 electric resistivity meter. During long periods of relatively little change (i.e., the background and streamflow monitoring periods), ERT measurements included the full acquisition dataset of 2853 measurements of voltage and resistance. A baseline resistivity tomogram representing an initial background condition for time-lapse ERT data was produced from 6 different ERT

data acquisitions during the spring of 2022, on 20 May (1 ERT dataset), 28 May (3 ERT datasets), 3 June (1 ERT dataset), and 4 June (1 ERT dataset) prior to streamflow arrival, by averaging the 6 background datasets (to minimize data noise attributed to high-contact resistance) and inverse modeling the averaged data. During the active filling of the channel in the streamflow arrival monitoring period, relatively short datasets containing 746 measurements were acquired because the shortened acquisition time of about 30 min enabled 7 ERT tomograms to be acquired in rapid succession over the course of about 3.5 h between 10:08 a.m. MDT and 13:44 p.m. MDT during the most transient period of streamflow conditions at the monitoring site.

The resistance measurements acquired during each individual ERT acquisition were filtered to remove anomalous noisy measurements (e.g., negative resistance values or values with large associated percent difference errors greater than 3 percent between repeated measurements); the resulting dataset was then processed through the Res2DInvx64 v4.06.23 inverse modeling software [30]. Inversion was performed using a least squares optimization procedure and a finite-element forward operation [62] to account for the topography of the ERT trench and obtain an inverted 2D resistivity model of the subsurface beneath the ERT trench that was iteratively changed from a homogeneous half-space model initial condition until the calculated resistance of the model closely matched that of the measured resistances within an acceptable error tolerance [63]. Additionally, the inversion procedure incorporated spatial weighting and roughness filters [64] to dampen the effects of noisy resistance measurements and temporal regularization to enforce smooth changes in the inverted resistivity tomograms through time [65,66].

The baseline resistivity tomogram, representing the background monitoring period prior to streamflow arrival, is shown in Figure 8 in addition to the resistivity tomogram acquired at the beginning of the streamflow monitoring period. The baseline tomogram in Figure 8a represents hydraulic conditions in the riverbed depicted in Figure 5a, whereas the final tomogram in Figure 8b represents hydraulic conditions at the beginning of the streamflow monitoring period. Tomograms acquired sequentially between the streamflow arrival and the streamflow monitoring periods were processed into tomograms showing the percent change in electric conductivity of the riverbed sediments, calculated from log-10-transformed values of the reciprocals of the inverted electrical resistivity distributions using Equation (8), as described by [11], where Δ_{EC}^{t} (percent) is the percent change in electric conductivity in the tomogram acquired at time index t (unitless), EC_{bulk}^{o} is the bulk electric conductivity distribution (S/m) in the baseline tomogram shown in Figure 8a (calculated as the reciprocal of the baseline resistivity distribution), and EC_{bulk}^{t} (S/m) is the conductivity distribution calculated from the electric resistivity tomogram acquired at time index *t*.

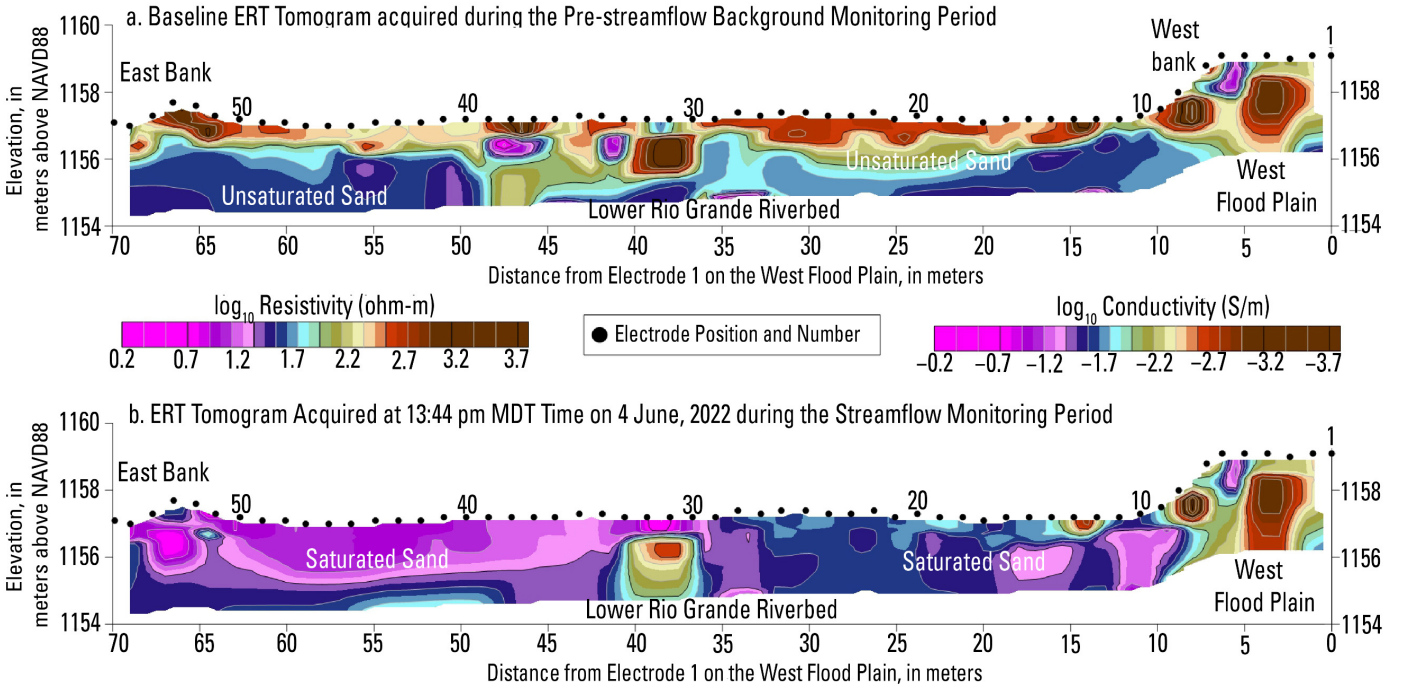

Figure 8. Electric resistivity tomograms acquired in the lower Rio Grande during the geoelectric monitoring survey. (**a**) Baseline ERT tomogram corresponding to the pre-streamflow background monitoring period reflecting conditions prior to 10:04 am MDT on 4 June 2022. (**b**) ERT tomogram acquired at 13:44 pm MDT on 4 June 2022 about 3.5 h after streamflow arrival at the monitoring site, corresponding to the beginning of the streamflow monitoring period.

$$\Delta_{EC}^{t} = 100 \times \frac{\left(EC_{bulk}^{t} - EC_{bulk}^{o}\right)}{EC_{bulk}^{o}} \quad (8)$$

3.3. Weather Data

Weather data were measured at the Chamberino weather station operated by Elephant Butte Irrigation District at coordinates 32.0622 N, 106.6788 W (WGS84 horizontal datum) approximately 1444 m due west from the geoelectric monitoring site on the flood plain of the west bank of the river (see Figure 1). The weather dataset consisted of measurements of surface air temperature, vapor pressure, and relative humidity at a height of 2.4 m above the land surface, soil temperature at a depth of 10 cm below the land surface, precipitation, wind velocity at a height of 3 m above the land surface, net incident solar radiation, and barometric pressure. The weather data were measured at 30 min intervals between 07:59 a.m. MDT on 21 May 2022 and 19:26 p.m. MDT on 4 September 2022 and used to compute a time-series model of potential evaporation (described in Appendix A) by using the combination model of [67] (see also [68–70]). The combination model combines a weighted estimate of potential evaporation attributed to near-surface energy balance variables with a weighted estimate of potential evaporation attributed to the aerodynamic mass flux of water vapor from the land surface [70–72]. Potential evaporation was computed for comparison with the voltage difference and electric potential time-series to evaluate the likelihood of streaming potential signals attributed to vertical capillary mass fluxes of soil moisture along a potential evaporation gradient in the Rio Grande riverbed and in the west flood plain.

The weather data used to calculate potential evaporation are shown in Figure 9 representing 30 min measurements of surface air temperature (Figure 9a), soil temperature (Figure 9b), precipitation (Figure 9c), relative humidity (Figure 9d), saturation vapor pressure (Figure 9e), mean wind speed (Figure 9f), net incident solar radiation (Figure 9g),

potential evaporation (Figure 9h), and barometric pressure (Figure 9i). The weather data are summarized in Table 1.

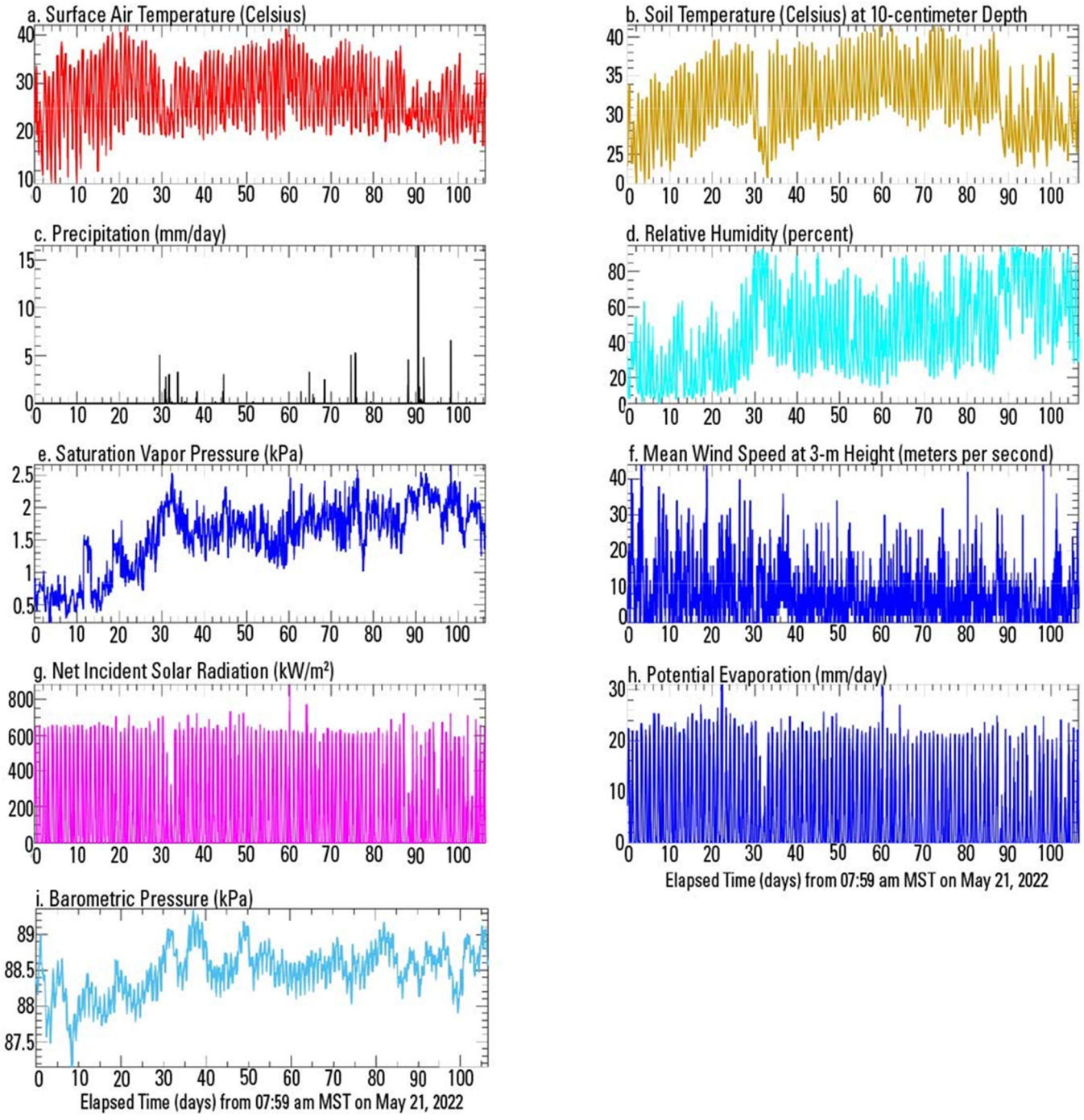

Figure 9. Time-series weather data [73] acquired from a weather station on the west flood plain about 1444 meters from the SP monitoring site including (**a**) surface air temperature in degrees Celsius; (**b**) soil temperature in degrees Celsius; (**c**) precipitation in millimeters per day; (**d**) relative humidity in percent; (**e**) saturation vapor pressure in kilopascals; (**f**) mean wind speed at a height of 3 meters above the land surface in meters per second; (**g**) net incident solar radiation in kilowatts per meter squared; (**h**) potential evaporation in millimeters per day, and (**i**) barometric pressure in kilopascals.

Table 1. Summary of time-series measurements of weather variables used to interpret the time-lapse SP monitoring data. Data used to compute the summary statistics shown in this table are provided in the corresponding U.S. Geological Survey data release ([73]).

Variable	Minimum	Maximum	Mean	Standard Deviation
Surface air temperature, in degrees Celsius	9.3	42	27.2	11.0
Soil temperature, in degrees Celsius	21.2	41.5	31.6	7.7
Precipitation, in millimeters per day	0	16.5	0.03	0.4
Relative humidity, in percent	5.3	94.9	46.7	22.9
Vapor pressure, in kilopascals	0.2	2.7	1.5	0.5
Average wind speed, in meters per second	0	98.3	17.2	3.5
Net solar radiation, in kilowatts per meter squared	0.0	882.6	184.3	228.4
Potential evaporation, in millimeters per day	0	31.0	6.6	8.1
Barometric pressure, in kilopascals	87.2	89.4	88.5	0.3

3.4. Hydrographic Data

Hydrographic data were provided by Elephant Butte Irrigation District (EBID) and used to aid in the interpretation of the SP monitoring data. The hydrographic data, plotted in Figure 10 and summarized in Table 2, consisted of 30 min measurements of streamflow in the lower Rio Grande at EBID Mesilla Cable river station no. 5 located at coordinates (32.2101 N, 106.7712 W) (WGS84 horizontal datum) about 3.2 km downstream from Mesilla Diversion Dam (about 19.8 km upstream from the geoelectric monitoring site) and GW-level elevation and depth-to-GW measurements in EBID monitoring well MES_23R located about 1411 m northwest from the geoelectric monitoring site on the east flood plain at coordinates (32.0678 N, 106.6495 W) (WGS84 horizontal datum). Streamflow and depth to groundwater were measured by following methods of [5,74,75]. The hydrograph data cover the majority of the geoelectric monitoring survey between 07:59 a.m. MDT on 21 May 2022 and 19:33 p.m. MDT on 4 September 2022. Hydrographic data are plotted in Figure 10 on a double vertical axis for ease of comparison. Individual monitoring periods referred to in Section 4 are annotated. Streamflow measurements (black series, left vertical axis) varied between no flow and 53.1 m^3/s; the mean streamflow was 19.5 m^3/s during the streamflow monitoring period. Continuous GW-level elevation data (gray series, right vertical axis), measured in the alluvial aquifer on the east flood plain, varied between 1155.8 m and 1156.4 m above NAVD88 datum, corresponding to a depth to GW in the observation well between 5.2 m and 4.6 m. The mean GW-level elevation during the geoelectric monitoring survey was 1156.1 m corresponding to a mean depth to GW of 5 m below the land surface.

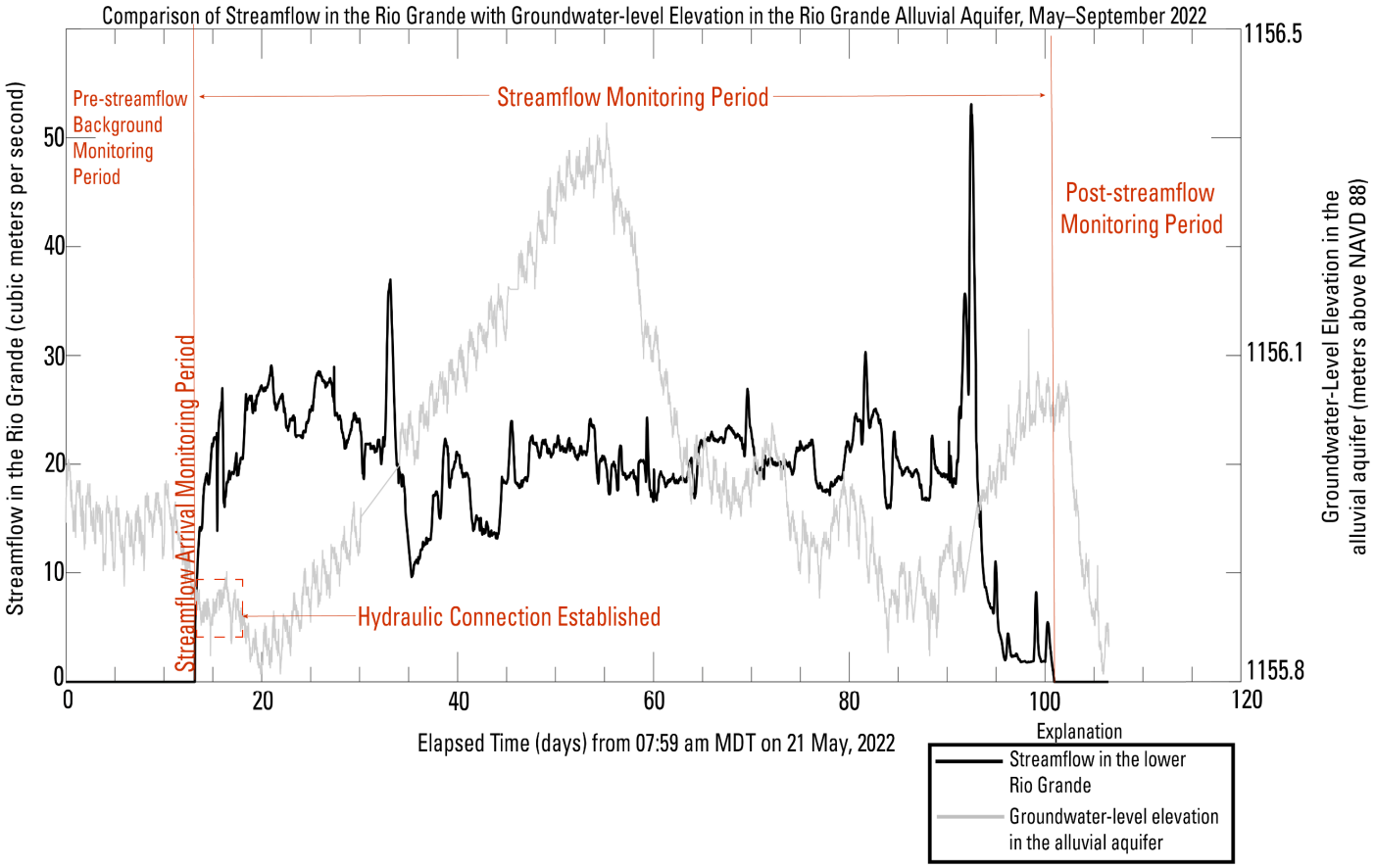

Figure 10. Hydrographic time-series data for streamflow in the lower Rio Grande at Elephant Butte Irrigation District (EBID) Mesilla Cable river station no. 5 between 07:59 a.m. MDT on 21 May 2022 and 19:33 p.m. MDT on 4 September 2022. GW-level elevations in EBID monitoring well MES_23R near the geoelectric monitoring site measured every 30 min between 07:59 a.m. MDT on 21 May 2022 and 19:54 p.m. MDT on 4 September 2022.

Table 2. Summary of continuous hydrographic data used to interpret the time-lapse SP monitoring data. Data used to compute the summary statistics shown in this table are provided in the corresponding U.S. Geological Survey data release ([73]).

Variable	Minimum	Maximum	Mean	Standard Deviation
Streamflow, in cubic meters per second	0	53.1	19.5	9.4
GW-level elevation, in meters above NAVD88	1155.8	1156.4	1156.1	0.13
Depth to GW, in meters	4.6	5.2	5	0.13

4. Results and Discussion

Four distinct monitoring time periods are represented in the geoelectric monitoring data, and each represents a different streamflow condition in the river. The distinct monitoring periods are (1) the "pre-streamflow background" monitoring period beginning at 07:59 a.m. MDT on 21 May 2022 and extending to about 10:04 am MDT on 4 June 2022, (2) the "streamflow-arrival" monitoring period beginning at 10:04 a.m. MDT on 4 June and encompassing a few hours thereafter as the streamflow arrived and began to infiltrate into the riverbed, (3) the "streamflow" monitoring period beginning at streamflow arrival on 4 June and encompassing the irrigation season to 21 August when upstream reservoir releases ended, and (4) the "post-streamflow" monitoring period, which began on 21 August and continued until 12:31 p.m. MDT on 4 October 2022.

Time-lapse photographs of the lower Rio Grande geoelectric monitoring site are shown in Figure 11 and depict the different monitoring periods annotated on the hydrograph in Figure 10. Figure 11a shows the lower Rio Grande riverbed on 15 May 2022, 6

days prior to streamflow arrival at the site. Figure 11b shows the streamflow arriving at the SP trench on 4 June 2022 from the ERT trench on the west bank looking from downstream to upstream. Figure 11c shows the monitoring site and river from the west flood plain on 16 August 2022, when streamflow was provided by reservoir releases from dams in upstream basins. The conditions shown in Figure 11c reflect the conditions of the streamflow monitoring period between June 4, when streamflow arrived at the site, and 21 August 2022, when reservoir releases at upstream dams ended. Figure 11d shows a photograph of the riverbed on 31 August 2022, 10 days after streamflow ended. Figure 11e shows a photograph of the riverbed on 4 October 2022, after the remaining SW in the riverbed infiltrated into the subsurface or evaporated into the atmosphere. Figure 11e shows the irrigated pecan orchards on the east bank near the monitoring site on 31 August 2022, which were flood-irrigated throughout the duration of the geoelectric monitoring survey.

Figure 11. Photographs of the of the lower Rio Grande riverbed and west and east flood plains pertaining to SP and ERT monitoring including (**a**) the lower Rio Grande riverbed on 15 May 2022, prior to streamflow arrival from upstream dam releases (taken by Scott Ikard, U.S. Geological Survey, looking downstream); (**b**) streamflow arrival on 4 June 2022 (taken by Chia-Hsing Tsai, New Mexico State University, looking upstream from the ERT trench towards the SP trench); (**c**)

streamflow conditions on 16 August 2022 (taken by Andrew Teeple, U.S. Geological Survey, from the west flood plain looking downstream towards the east bank); (**d**) streamflow conditions on 31 August 2022 after streamflow provided by upstream dam releases had ended (taken by Kenneth Carroll, New Mexico State University, looking downstream); (**e**) riverbed on 4 October 2022, (taken by Scott Ikard, U.S. Geological Survey, from the west flood plain looking northeast); and (**f**) flood-irrigated pecan orchards on the east flood plain (see also Figure 5a) on 31 August 2022 (taken by Kenneth Carroll, New Mexico State University).

4.1. Pre-Streamflow Background Condition Monitoring Period

Figure 12 shows SP monitoring data measured during the pre-streamflow background monitoring period. Figure 12a depicts the time-series of processed voltage differences between each electrode and the reference (electrode 1), processed by applying drift corrections and performing recursive notch filtering to remove the 1-cycle-per-day and 2-cycles-per-day sinusoids as described in Section 3.1 of this paper. Figure 12b depicts the corresponding electric potential time-series at each electrode obtained by numerically integrating the time-series data in Figure 12a through time with Equation (7). Spatial profiles of the time-series data are shown in Figure 12c,d (at an arbitrary time indicated by the vertical black bar in Figure 12a,b). The maximum, minimum, and mean values of the voltage difference and electric potential time-series data at each electrode are depicted by the light gray lines. The electric potential time-series in Figure 12b are almost exclusively positive for the entirety of the pre-streamflow background monitoring period, and the electric potential profile across the channel in Figure 12d depicts a relatively smooth increase from the reference electrode on the west flood plain into a strong positive anomaly in the riverbed. The positive electric potential anomaly in the riverbed increases towards the east bank of the river and achieves a peak magnitude in excess of +100 mV between 7 and 8 days after the start of monitoring.

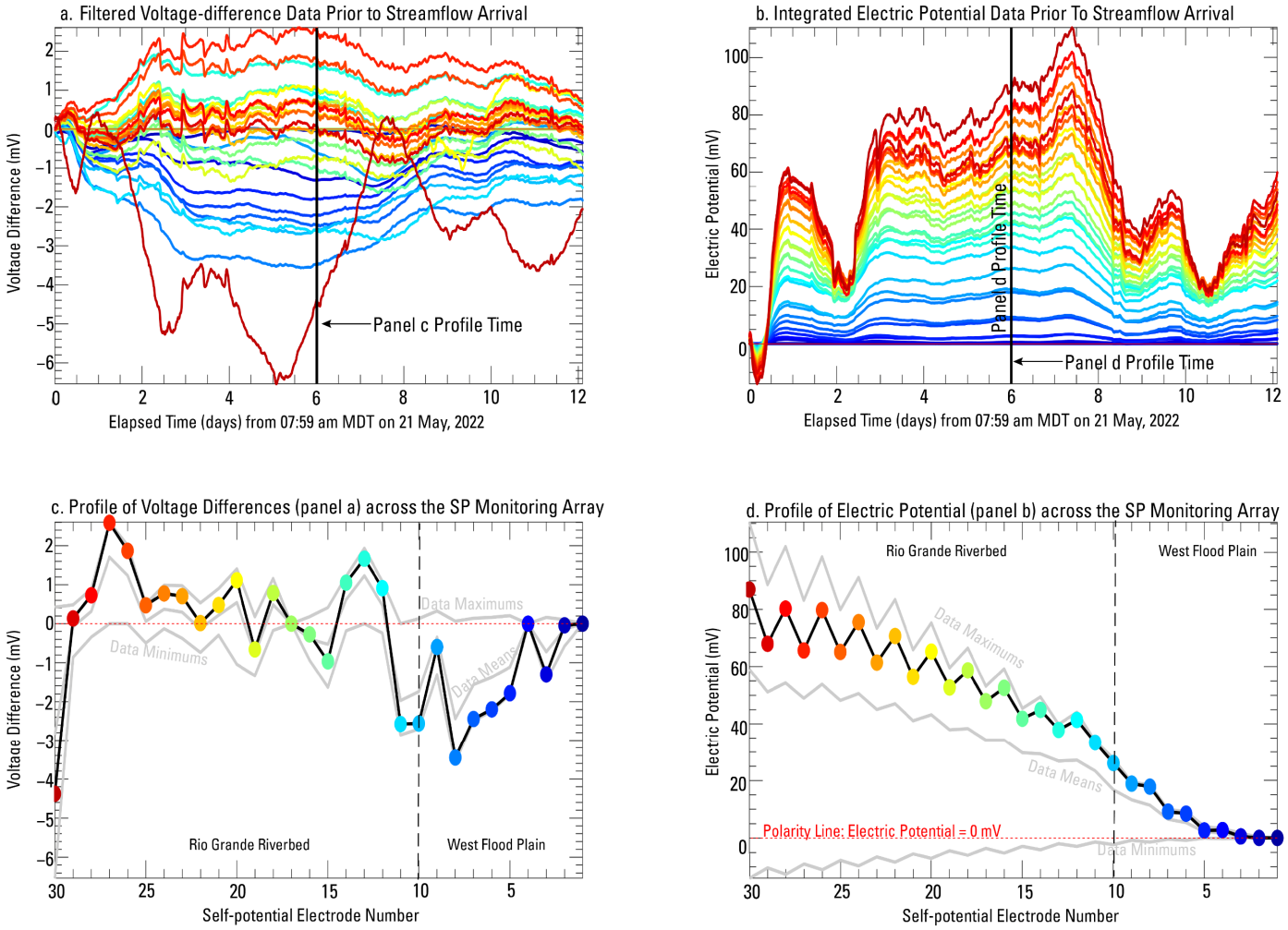

Figure 12. Time-lapse SP data measured across the Rio Grande riverbed and west flood plain during the background monitoring period beginning 21 May 2022 at 07:59 am Mountain Daylight Time (MDT) and ending at 10:21 am MDT on 2 June 2022. (**a**) Time-series of drift-corrected voltage differences. (**b**) Time-series of electric potential calculated from data in panel (**a**). (**c**) Profile of voltage differences at each electrode relative to electrode 1 at the arbitrary time indicated by the vertical black line in panel (**a**). The gray lines indicate the minimum, maximum, and mean values of the time-series voltage differences measured at each electrode shown in panel (**a**). (**d**) Profile of electric potential at each electrode at the arbitrary time indicated by the vertical black line in panel (**b**). The gray lines indicate the minimum, maximum, and mean values of the time-series electric potential at each electrode shown in panel (**b**). Colors indicate the spatial position of the measured time-series in the SP electrode array, and correspond to numbered SP electrodes depicted in Figure 5.

The electric potential profile data in Figure 12d support the intuitive observation that the background condition in the riverbed is one of hydraulic disconnection (there is no streamflow, and the depth to GW in monitoring well MES-23R is greater than 4.9 m during the pre-streamflow monitoring period). The electric potential profile data measured during the pre-streamflow monitoring period therefore support the hypothesis that the background electric potential anomaly in the riverbed is predominantly a diffusion potential attributed to a vertical salt concentration gradient beneath the land surface at the monitoring site. Cationic diffusion along a concentration gradient oriented vertically upwards beneath the land surface in the Mesilla Basin could result in a positive diffusion potential anomaly at the land surface when streaming potential and thermoelectric potential effects are absent. This would explain the positive increase in electric potential towards the east bank, which may reflect stronger near-surface concentration gradients attributed to agricultural irrigation on the east bank [55].

This hypothesis is further supported by a number of relevant previous studies. For example, ref. [53] showed that anomalous changes in SW temperature and specific conductance data occurred at the geoelectric monitoring site and were spatially coincident with a strong near-surface vertical resistivity contrast. SW near the geoelectric monitoring site was characterized by higher specific conductance and lower temperature relative to the specific conductance and temperature of the SW at seepage station S01 (Figures 1 and 2). The SW specific conductance deviations were consistent with pattern 3 depicted in Figure 4. In [53], the authors also interpreted an apparent diffusion potential attributed to an ionic diffusion along a vertical salinity gradient near seepage stations S16 and S17 (Figures 1 and 2) a few kilometers upstream from the monitoring site. The electric potential profile in Figure 2a generally represented the streamflow gain/loss curve well in terms of similar spatial variations, although the profile data between seepage stations S16 and S17 indicated an apparent gain, whereas the streamflow gain/loss curve depicted a losing condition between S16 and S17. Spatially coincident resistivity profiles at depths of 3.5 m and 50 m beneath the riverbed (Figure 2b) showed that vertical contrast from high to low resistivity with increasing depth was also present beneath the riverbed near stations S16 and S17, and SW specific conductance deviations near stations S16 and S17 also were consistent with pattern 3 depicted in Figure 4. Ikard et al. [53] therefore concluded that diffusion of a cationic species along a vertical salt concentration gradient was a plausible cause for the discrepancy between the electric potential and the streamflow gain/loss curve.

Furthermore, through an analysis of legacy temperature data and GW flux estimates, ref. [56] indicated that known geothermal systems in the Mesilla Basin, including one of the largest known cold-temperature geothermal systems in the U.S., may contribute more than 45,000 tons of dissolved solids per year to the shallow aquifer system, with about 18% being delivered from localized groundwater upwelling zones within the geothermal systems. Faults throughout the basin may allow upward leakage of saline water from depths greater than 1 km into the Santa Fe Group and downward or lateral leakage of freshwater from the alluvial aquifer into the Santa Fe Group [54], creating a vertical concentration gradient in the near-surface of the basin. While the resistivity profile data in Figures 1 and 2 do not indicate a substantial resistivity contrast between depths of 0 and 50 m beneath the monitoring site, the resistivity depth slices in Figure 3 indicate that a much stronger resistivity contrast occurs between depths of 0 and 457 m in the basin a few kilometers to the south of the monitoring site location.

4.2. Streamflow Arrival Monitoring Period

SP monitoring data were not acquired during the streamflow arrival monitoring period as explained in Section 3.1; however, time-lapse ERT data were acquired during the streamflow arrival monitoring period. A total of 7 ERT tomograms were acquired in rapid succession between 10:08 a.m. MDT and 13:44 p.m. MDT as the streamflow arrived and infiltrated into the riverbed. Percent changes in the conductivity of the riverbed sediments relative to the ERT tomogram produced from ERT data acquired during the pre-streamflow background monitoring period (Figure 8) are shown in Figure 13. Figure 13a shows that the conductivity of the near-surface sediments increases relative to the background condition nearly instantaneously upon streamflow arrival—a finding that was observed also by [11] at their monitoring site upstream. Electric conductivity increases generally from east to west in successive tomograms, presumably based on existing preferential SW flow paths in the riverbed during streamflow arrival. In successive tomograms (Figure 13b–g), the conductivity of the subsurface beneath the ERT trench increases at successively greater depths as the streamflow infiltrates into the alluvial aquifer. Increases in the electric conductivity of the riverbed through time can be attributed exclusively to changes in the temperature and effective saturation of the riverbed sediments that occurred between completely dry and completely saturated conditions. Increases in percent change in riverbed conductivity values greater than zero in successive tomograms through time indicate that the riverbed is becoming increasingly saturated, and consequently, only

losing conditions are possible during the streamflow arrival monitoring period. This finding was observed also by [11], who noted that similar observations suggested rapid mixing and cycling within the hyporheic zone of their monitoring site, leading to full hydraulic connection at their monitoring site within 24 h.

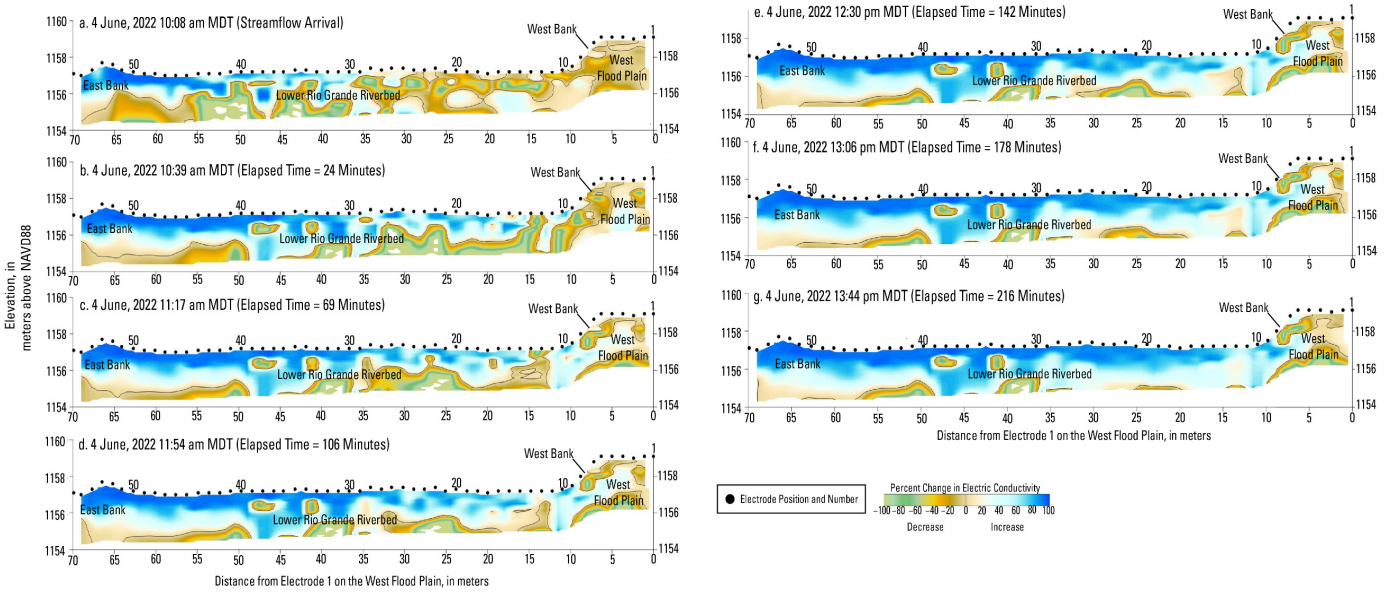

Figure 13. Time-lapse ERT monitoring data acquired during the streamflow arrival monitoring period beginning at 10:08 a.m. Mountain Daylight Time (MDT) on 4 June 2022. Tomograms show the percent change in electric conductivity relative to the conductivity distribution converted from the resistivity distribution depicted in the background tomogram acquired on 3 June 2022, during the background monitoring period. (**a**) Time of 10:08 a.m., 0 min after streamflow arrival. (**b**) Time of 10:39 a.m., 24 min after streamflow arrival. (**c**) Time of 11:17 a.m., 69 min after streamflow arrival. (**d**) Time of 11:54 a.m., 106 min after streamflow arrival. (**e**) Time of 12:30 p.m., 142 min after streamflow arrival. (**f**) Time of 13:46 p.m., 178 min after streamflow arrival. (**g**) Time of 13:44 p.m., 216 min after streamflow arrival.

According to [11], the point at which the river–aquifer system transitions from hydraulically disconnected to hydraulically connected occurs when the GW table beneath the river is mounded with the river stage demarcating the highest GW table elevation. The GW-level hydrograph in Figure 10 indicates that the depth to GW in the alluvial aquifer on the east flood plain was in the range of 4.6–5.2 m (corresponding to groundwater-level elevations between 1210.7 m and 1211.3). ERT tomograms in Figure 13 show that conductivity is increasing at a depth of about 3 m beneath the riverbed, including Figure 13g at 13:44 p.m. MDT (elapsed time of 216 min, or 12,960 s after streamflow arrival), providing a rough estimate of the infiltration rate of about 2.3×10^{-4} m/s. This estimate is comparable to the range of horizontal hydraulic conductivity of the alluvial aquifer reported by [54], which was 4×10^{-4}–1.2×10^{-3} m/s. Percent change tomograms in Figure 13 indicate that the hydraulic connection between the streamflow in the lower Rio Grande and the GW in the alluvial aquifer occurs rapidly, on the order of several hours after the streamflow arrival. This is further indicated by the relative increases in GW-level elevation shown in Figure 10 that occur almost instantaneously with the arrival of streamflow upstream (between an elapsed monitoring time of about 12 and 15 days) and again between about 20 days and 50 days when the GW level in the observation well achieves the maximum elevation.

4.3. Streamflow Monitoring Period

Self-potential monitoring was re-established on 8 June 2022, at 10:00 a.m. MDT, about 4 days after the streamflow arrival on 4 June. At this time, the time-lapse ERT data in Figure 13 and GW-level elevation data in Figure 10 indicated that the hydraulic

connection between the Rio Grande and the alluvial aquifer was likely established. The full time-series of voltage difference and electric potential monitoring data are shown in Figure 14a,b, respectively, and corresponding spatial profiles of voltage differences and electric potential across the riverbed are shown in Figure 14c,d, respectively, at the time indicated by the vertical black bars. Gaps in the SP monitoring data are indicated by the horizontal lines between the dashed vertical black lines in panels a–b. Having removed the 1-cycle-per-day and 2-cycles-per-day sinusoids from the voltage difference time-series, the SP monitoring data show the change in the voltage differences and electric potential field during the streamflow and post-streamflow monitoring periods relative to the pre-streamflow background monitoring period. The time-series of voltage differences and electric potential depicted in Figure 14a,b show the background condition prior to June 2, where the electric potential time-series data are predominantly positive-valued, followed by a polarity change from positive to negative polarity relative to the background monitoring condition at streamflow arrival. A comparison of the streaming potential data in Figure 14b with the streamflow hydrograph in Figure 10 shows that the polarity switch and decrease through time are nearly coincident in time with the arrival of streamflow at the upstream gage. This polarity change attributed to streamflow arrival initiated a transient, slow, gradual decrease in electric potential in each SP electrode that persisted through the streamflow and post-streamflow monitoring periods. The profile of voltage differences across the riverbed in Figure 14c appears noisy with predominantly positive values over the riverbed and larger amplitudes in riverbed electrodes relative to electrodes in the west flood plain. In contrast, the profile of electric potential across the riverbed shows a negative electric potential anomaly in the riverbed that decreases smoothly and gradually from the reference electrode on the west flood plain across the riverbed to electrode 30 at the base of the east bank. The maximum, minimum, and mean values of the time-series data are plotted as profiles by the light gray lines in Figure 14c,d and show that the electric potential anomaly in the riverbed achieves a minimum amplitude of −3500 mV during the SP monitoring period.

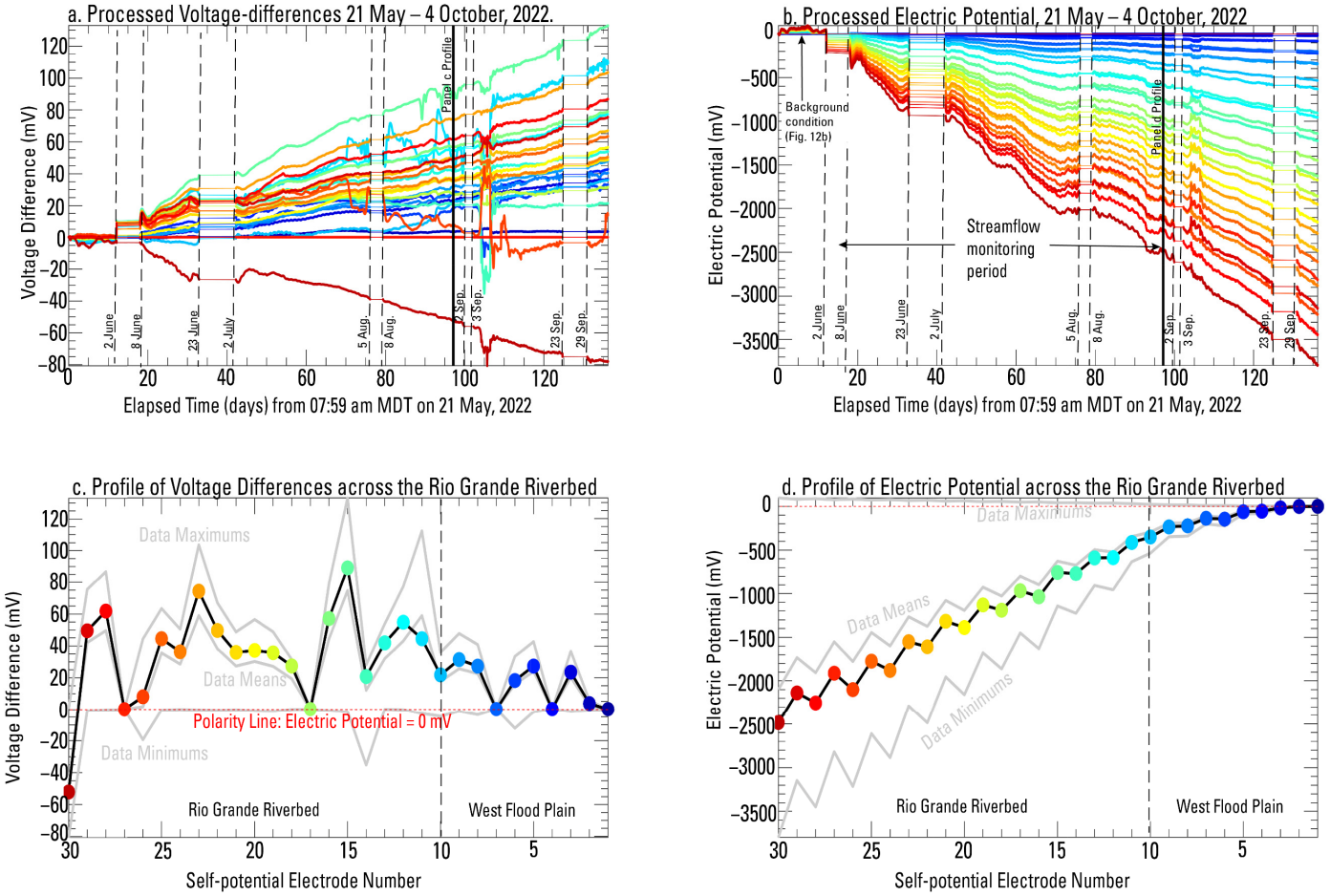

Figure 14. Time-lapse SP data measured across the Rio Grande riverbed and west flood plain beginning on 21 May 2022 at 7:59 a.m. MDT and ending on 4 October 2022. (**a**) Time-series of drift-corrected voltage differences. (**b**) Time-series of electric potential calculated from data in panel (**a**). (**c**) Profile of voltage differences at each electrode relative to electrode 1 at the arbitrary time indicated by the vertical black line in panel (**a**). The gray lines indicate the minimum, maximum, and mean values of the time-series voltage differences measured at each electrode shown in panel (**a**). (**d**) Profile of electric potential at each electrode at the arbitrary time indicated by the vertical black line in panel (**b**). The gray lines indicate the minimum, maximum, and mean values of the time-series electric potential at each electrode shown in panel (**b**). Colors indicate the spatial position of the measured time-series in the SP electrode array, and correspond to numbered SP electrodes depicted in Figure 5.

Similar to the ERT data acquired during the streamflow arrival monitoring period, the electric potential time-series and profile data shown in Figure 14 indicate that the lower Rio Grande experiences exclusively losing conditions during the streamflow monitoring period. This is evident by comparing the electric (streaming) potential time-series in Figure 14b to the numerical simulations of electrokinetic fields in rivers attributed to streamflow gaining, losing, and flow-through conditions, published by [76–78]. Notably, the simulated electric potential profiles from the purely losing models of [76,77] appear remarkably similar to the electric potential profiles shown in Figure 14d in terms of polarity and spatial appearance from the flood plain into the riverbed. While there are no obvious indications of flow-through in the electric potential profile data in Figure 14d, as represented in the numerical simulations of [76–78], the general character of the electric potential profile in Figure 14d indicates that the lower Rio Grande may be losing more SW on the east bank than on the west bank by the steady negative decrease in the electric potential profile from the west flood plain towards the east bank. This may be the result of flood-irrigated pecan orchards on the east flood plain (Figure 11e). Flood irrigation by

GW withdrawal may create a drawdown cone and slope the phreatic surface towards the east flood plain beneath the riverbed, drawing more SW into the east flood plain relative to the west flood plain and resulting in the periodic fluctuations observed in the GW-level elevation data in Figure 10 as the irrigation water is withdrawn and infiltrated back into the alluvial aquifer.

4.4. Post-Streamflow Monitoring Period

SW releases from upstream dams ended on about 21 August 2022, approximately 100 days after the monitoring survey began (Figure 10), marking the beginning of the post-streamflow monitoring period. Several days prior (92–94 days after monitoring began), streamflow decreased abruptly from the maximum streamflow to about 2 m^3/s and remained relatively constant for approximately 5 days until streamflow was again reduced to 0 m^3/s, as shown in Figure 10.

Figure 15 shows voltage difference and electric potential time-series and associated profiles across the river during the post-streamflow monitoring period when hydraulic conditions were as depicted in Figure 11c,d. The effect of reduced streamflow is observed rapidly in the electric potential time-series data shown in Figure 15b, where the decreasing electric potential behavior in Figure 14b reverses to a brief period of transient increase followed by another reversal to transient decreasing behavior similar to the streamflow monitoring period depicted in Figure 14b. This increasing and decreasing electric potential behavior, observed between elapsed times of 95 and 100 days, is attributed to a brief period of return flows from the flood plain into the river as the horizontal hydraulic gradients equalized, followed by continued SW loss from the river into the alluvial aquifer between about 101 and 105 days after monitoring began. The electrical instability observed in each time-series in Figure 15b between about 105 and 107 days may be an effect of pressure head equalization within the alluvial aquifer as the river–aquifer system transitions between hydraulic connection and disconnection; however, the transient electric potential data have not been modeled in the context of this process, and this is merely a hypothesis based upon the observations.

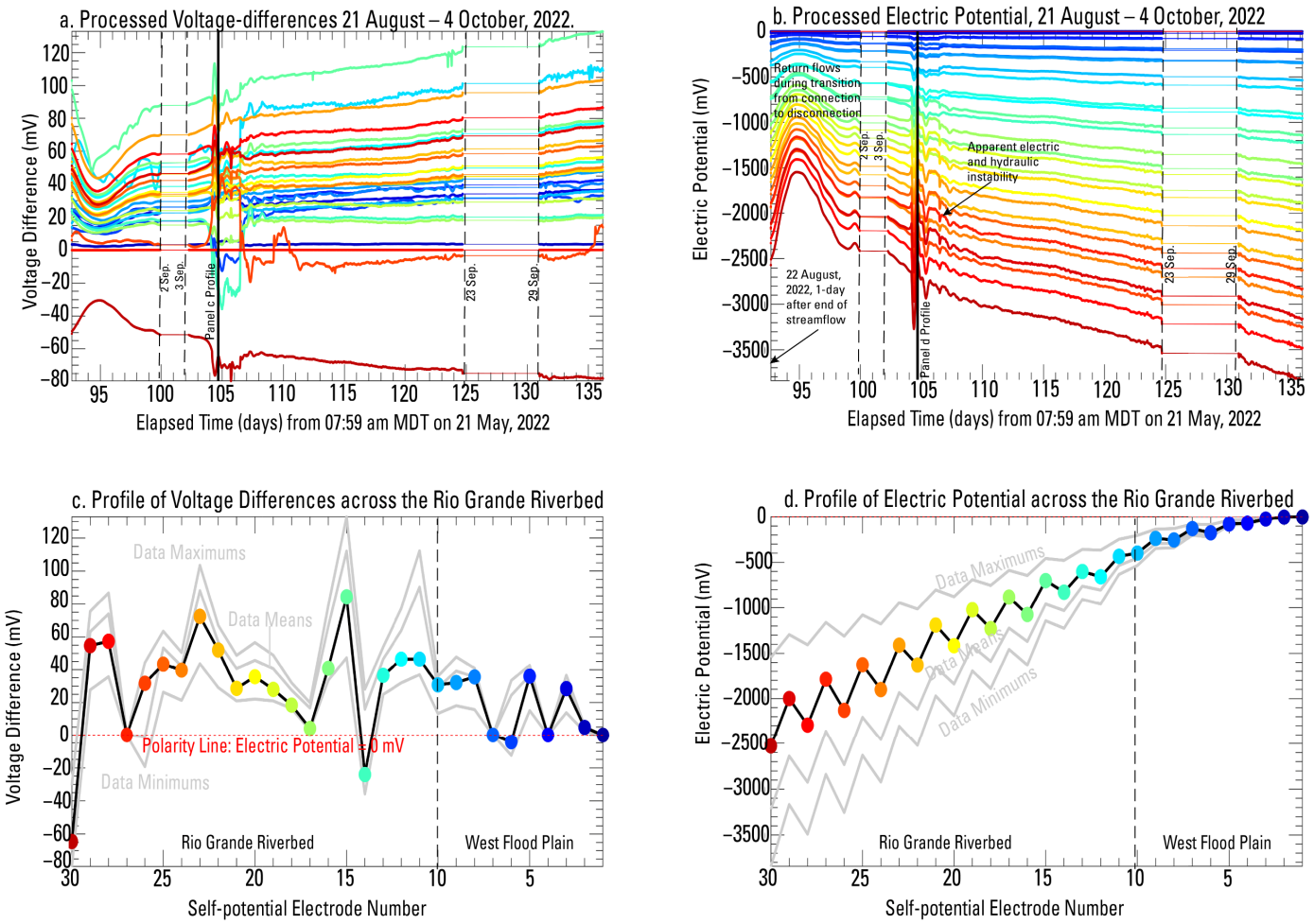

Figure 15. Time-lapse SP data measured across the Rio Grande riverbed and flood plain on the west bank during the post-streamflow monitoring period. The data depicted cover the period of monitoring time beginning on 21 August 2022 and ending on 4 October 2022 at 12:31 pm MDT. (**a**) Time-series of drift-corrected voltage differences. (**b**) Time-series of electric potential calculated from data in panel (**a**). (**c**) Profile of voltage differences at each electrode relative to electrode 1 at the arbitrary time indicated by the vertical black line in panel (**a**). The gray lines indicate the minimum, maximum, and mean values of the time-series voltage differences measured at each electrode shown in panel (**a**). (**d**) Profile of electric potential at each electrode at the arbitrary time indicated by the vertical black line in panel (**b**). The gray lines indicate the minimum, maximum, and mean values of the time-series electric potential at each electrode shown in panel (**b**). Colors indicate the spatial position of the measured time-series in the SP electrode array, and correspond to numbered SP electrodes depicted in Figure 5.

After about 107 days, the post-streamflow voltage difference and electric potential time-series data change slowly and gradually, and the slope of the time-series is reduced relative to earlier times. This implies that the return to the background condition is likely to be a slow process as the riverbed sediments dry out. Figure 11 depicts this process through photos of streamflow conditions on 16 August (Figure 11b, presumed comparable to 21 August streamflow conditions) and the conditions shown in the riverbed on 31 August (Figure 11c) when there is still infiltrating SW ponded in the riverbed, ten days after upstream reservoir releases ended.

4.5. Analysis of Diurnal Electric Potential Fluctuations

The diurnal electric potential fluctuations calculated with Equation (7) from the diurnal voltage difference fluctuations filtered from the raw data (Figure 7g) are shown in Figure 16. These fluctuations were analyzed to determine the underlying source of

fluctuation. Figure 16a shows diurnal electric potential fluctuations measured during the pre-streamflow background monitoring period, and Figure 16b shows electric potential fluctuation measured between 8 and 23 June 2022 during the streamflow monitoring period. Notable differences are evident between fluctuations during the two monitoring periods, both spatially and temporally. In a spatial sense (refer to the color-coding in Figure 5), fluctuations during the streamflow monitoring period display a clear difference beneath the riverbed compared to those that occur in the west flood plain. In a temporal sense, fluctuations during the streamflow monitoring period show a pronounced change relative to those that occur during the pre-streamflow background monitoring period in terms of an amplitude reduction and spatial appearance—a likely result of the presence of surface-water in the riverbed during the streamflow monitoring period. Diurnal electric potential fluctuations varied between minimum and maximum values of about −30,000 mV and +25,000 mV at SP electrodes 1–29 and between values of about −70,000 mV and +25,000 mV for SP electrode 30 data during the pre-streamflow monitoring period and oscillated between positive and negative polarity. In contrast, during the streamflow monitoring period, amplitudes varied between minimum values of about −1500 mV and maximum values of about +1500 mV, and the electric potential fluctuations in riverbed electrodes appear to retain predominantly positive polarity, with the exception of the electrode 30 data.

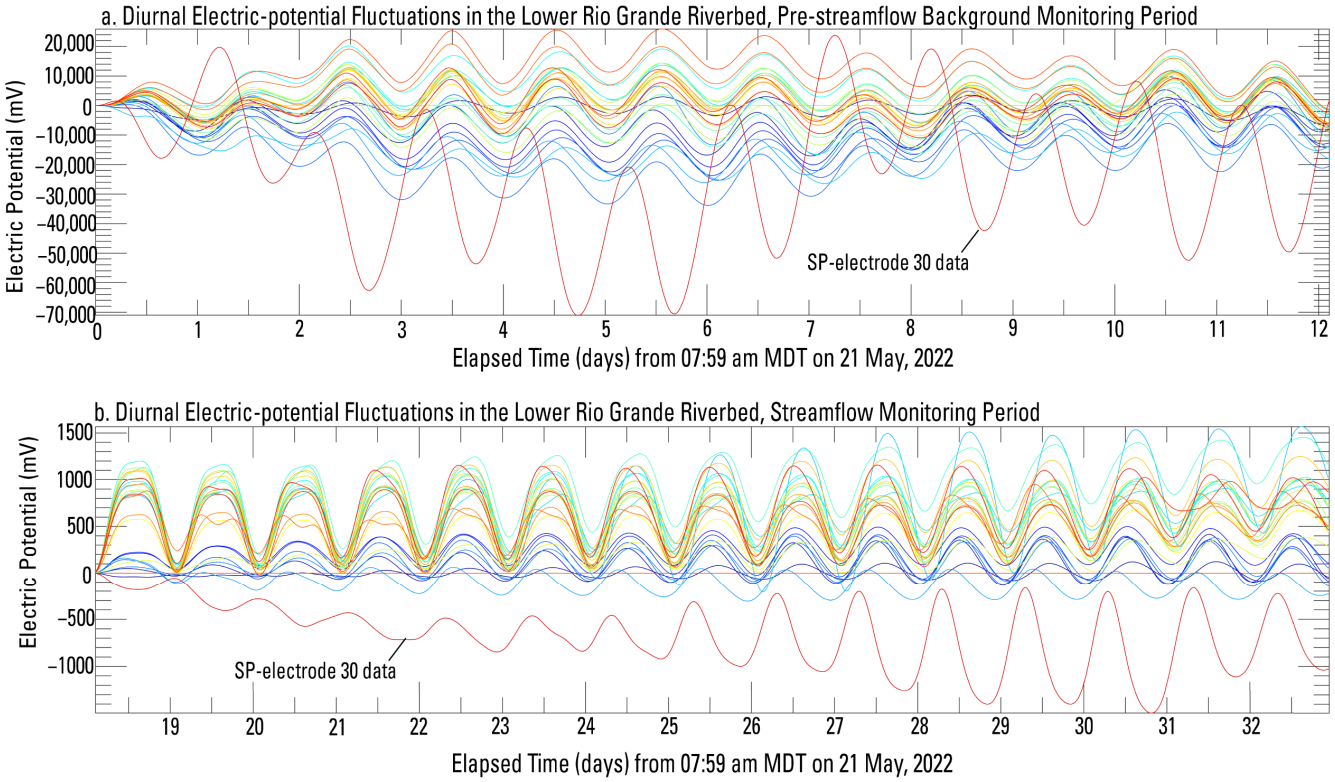

Figure 16. Comparison of the diurnal electric potential fluctuations calculated from diurnal voltage differences extracted from the pre-streamflow monitoring period and streamflow monitoring period self-potential data by notch filtering. (**a**) Diurnal electric potential fluctuations corresponding to the background monitoring period. (**b**) Diurnal electric potential fluctuations corresponding to approximately 15 days of the streamflow monitoring period between 8 June and 23 June 2022. The streamflow conditions in the river corresponding to each monitoring period are depicted in Figure 11. Colors indicate the spatial position of the measured time-series in the SP electrode array, and correspond to numbered SP electrodes depicted in Figure 5.

Three plausible sources of the diurnal electric potential fluctuations depicted in Figure 16 were considered. The first plausible source was diurnal temperature fluctuation, which can produce diurnal electric potential fluctuations based on the temperature

coefficient of the electrodes and the temperature difference between each electrode and the reference electrode. However, this was logically ruled out because the temperature coefficient of the SP electrodes is roughly 0.5 mV/°C [79] and the diurnal voltage difference fluctuations shown in Figure 7g vary between about 2 and 4 mV. Voltage difference fluctuations in that range would require temperature differences between SP electrodes in the range of 4–8 °C, which is unreasonably large over the short distances between the electrodes and the short length of the SP monitoring array. These findings are consistent with those of [22], who observed anomalous diurnal voltage difference fluctuations that appeared suddenly in summer months at an SP monitoring site in Garchy, France, and varied in magnitude between 0.1 mV and 1.5 mV. Observations by [22] were comparable to, but generally less than, the amplitudes of the diurnal voltage differences shown in Figure 7g. They concluded that the amplitudes of the variations were not consistent with a thermal effect imparted upon the data logging instrumentation and were too large to be consistent with an effect based on the temperature coefficients of the lead-chloride monitoring electrodes that they used. Interestingly, and similar to the data herein, they noted spatial variations whereby the amplitudes of their so-called diurnal thermal wave increased from the west of their monitoring site towards the east. Because of the spatial coherency that they observed in diurnal voltage difference variations, ref. [22] concluded that the diurnal variations were therefore a coherent signal rather than a localized effect of temperature on individual electrodes.

The second plausible source considered was that diurnal electric potential fluctuations were streaming potentials attributed to diurnal variability in the vertical potential evaporation gradient in the alluvial aquifer sediments, related to diurnal changes in incident solar radiation imparted by the rising and setting sun. Potential evaporation calculated from weather data (Figure 9) was compared to the diurnal electric potential fluctuations to determine whether the underlying causative source could be reasonably attributed to a vertical capillary mass flux of soil moisture beneath the riverbed. Figure 17 compares weather data in Figure 9 with diurnal electric potential fluctuations in Figure 16a. Figure 17a compares maximum normalized net solar radiation (pink), surface air temperature (red) and soil temperature (bronze), and potential evaporation (blue) with electric potential fluctuations at SP electrode 20 (yellow, located in the center of the riverbed) and shows an enlarged 3-day-long time window of data during the pre-streamflow background monitoring period.

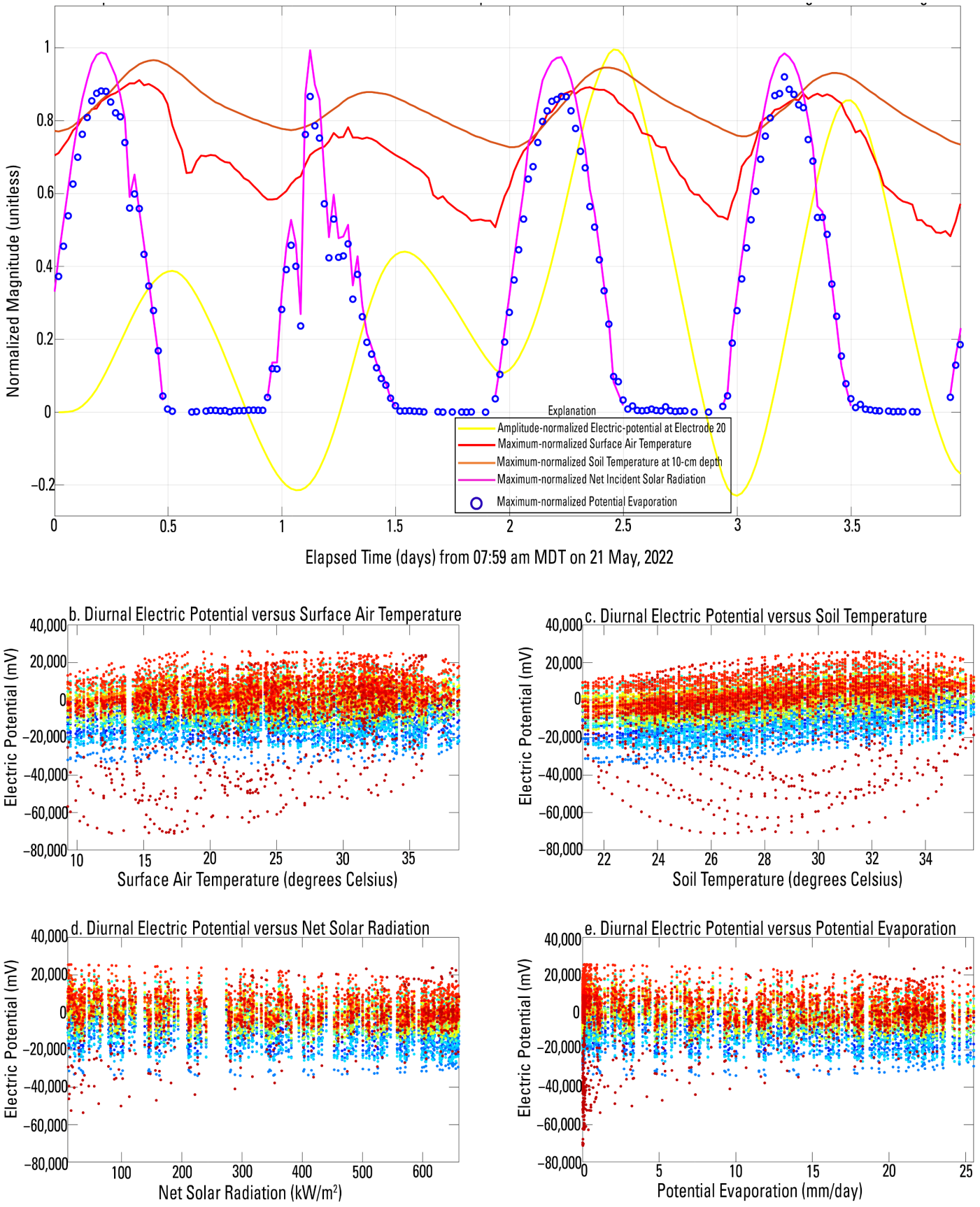

Figure 17. (**a**) Comparison of normalized weather data time-series with amplitude-normalized diurnal electric potential at self-potential electrode 20. (**b**) Scatter plot of diurnal electric potential versus surface air temperature. (**c**) Scatter plot of diurnal electric potential versus soil temperature. (**d**) Scatter plot of diurnal electric potential versus net solar radiation. (**e**) Scatter plot of diurnal electric

potential versus potential evaporation. Colors in panels (**b**)–(**e**) indicate the spatial position of the measured time-series in the SP electrode array, and correspond to numbered SP electrodes depicted in Figure 5.

Figure 17a indicates that net radiation and potential evaporation are in phase such that the peak solar radiation corresponds to peak potential evaporation. Peaks in surface air temperature are phase-shifted relative to solar radiation and potential evaporation, and peaks in soil temperature are phase-shifted relative to peaks in surface air temperature, illustrating a transfer of heat energy from the atmosphere into the ground. Notably, the maximum and minimum diurnal electric potential fluctuations at SP electrode 20 appear to be most collocated in time to the maximum and minimum values of soil temperature, although a slight phase shift between the electric potential and soil temperature fluctuations is also evident. It appears that the maximum electric potentials are collocated in time with the onset of sundown (the end of the decreasing limb of the net radiation curve), and the minimums of the electric potential fluctuations are correlated in time to sunrise (the beginning of the increasing limb of the net radiation curve). The decreasing limb of electric potential fluctuations appears to follow the peak of the net radiation and potential evaporation curves, an observation that contradicts the streaming potential source but supports the concept that heat flux in the near-surface is driving the decreasing trends on a daily basis. Streaming potentials attributed to potential evaporation driven by net radiation were ultimately ruled out as a source based on the scatterplots of diurnal electric potential fluctuations and weather variables in Figure 17b–e, which indicate that diurnal electric potential fluctuations show mild discernable correlation with surface air temperature (Figure 17b) and soil temperature (Figure 17c) and little to no discernible correlation to net radiation (Figure 17d) and potential evaporation (Figure 17e). Furthermore, it is counterintuitive to expect that vertical mass flux of soil moisture would produce a streaming potential anomaly that exceeds a 40,000 mV amplitude daily, whereas the sustained losses of streamflow in the lower Rio Grande over several months during the irrigation season would only produce an electric potential anomaly of about −3500 mV. The diurnal electric potential fluctuations measured at the monitoring site were therefore attributed to heat conduction through the soil and are considered thermoelectric in origin. Support for this is offered by the experimental laboratory results of [26] who showed through self-potential monitoring of thermal pulse convection in a sand tank that increases in subsurface temperature attributed to the flow of heat energy was a direct cause for the transient growth of negative self-potential anomalies over the heat-flow path.

The diurnal electric potential fluctuations in Figure 16 display temporal and spatial coherence, similar to observations made by [22], and present themselves spatially as a transient wave in the electric potential field at the monitoring site. Figure 18 shows the diurnal voltage difference (Figure 18a) and electric potential (Figure 18b) fluctuations during the background monitoring period in addition to spatial profiles of the data at two different times within one cycle (Figure 18b–e). The range of the profile data shown by the minimum and maximum lines (gray lines) shows that diurnal fluctuations display spatial coherence in the form of propagation of a wave in the electric potential field, which has a maximum spatial amplitude of about +2000 mV through time, from west to east across the monitoring array. When plotted continuously through time, the anomalous behavior of voltage difference and electric potential fluctuations at electrode 30 (relative to those at electrodes 2–29) observed in Figures 5b,c, 8, and 16 appears related to the wavelength of the observed wave. Given the spatial and temporal comparisons of the diurnal electrical potential variations described herein, and their notably large amplitudes, it is concluded that the diurnal electric potential variations observed in the data depict transient thermoelectric waves attributed to heat conduction through the flood plain and riverbed sediments. The spatial and temporal changes in the electric potential time-series in Figure 16 between pre-streamflow and streamflow monitoring periods are therefore a likely and plausible result of the change in thermal conductivity between the unsaturated and

saturated riverbed sediments in the background monitoring and streamflow monitoring periods, respectively. According to [80], representative values of thermal conductivity for unconsolidated porous geologic sediments can vary around 0.18 W/m·K for dry sediments and between 1.4 W/m·K and 2.2 W/m·K for saturated sediments, corresponding to roughly an order of magnitude increase. The saturated riverbed sediments therefore enhance near-surface heat conduction relative to the unsaturated conditions by the change in thermal conductivity that occurs between dry and saturated conditions.

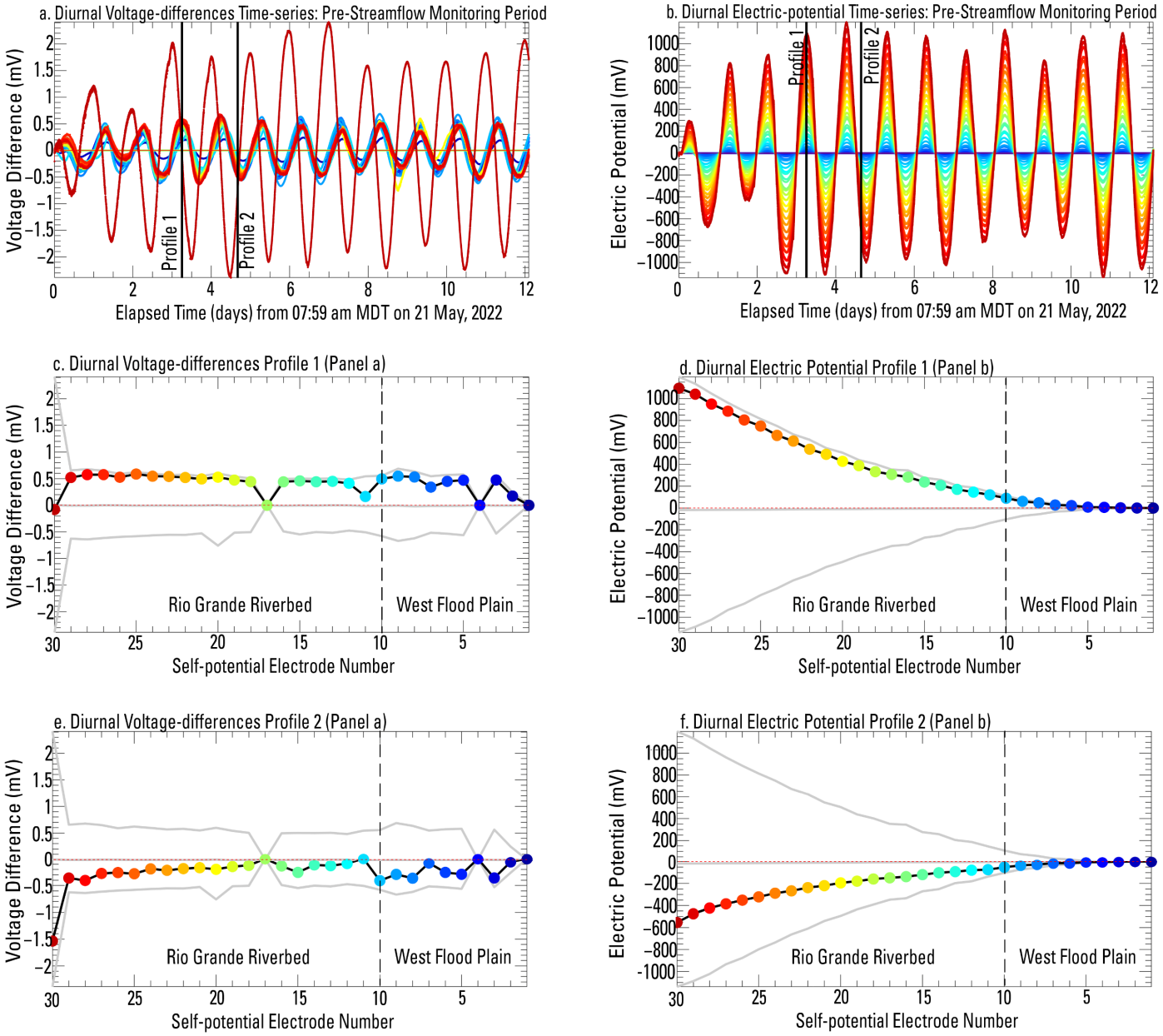

Figure 18. Comparison of 1-cycle-per-day periodic fluctuations in drift-corrected voltage difference and electric potential time-series with spatial profiles across the west bank and riverbed at two arbitrary times within the background monitoring period. (**a**) One-cycle-per-day periodic fluctuations in drift-corrected voltage difference time-series. (**b**) One-cycle-per-day periodic fluctuations in electric potential time-series corresponding to the voltage differences in panel (**a**). (**c**) Spatial profile of 1-cycle-per-day period fluctuations of voltage difference time-series at arbitrary time t1 depicted by the black vertical bar in panel (**a**). (**d**) Spatial profile of 1-cycle-per-day period fluctuations of electric potential time-series at arbitrary time t1 depicted by the black vertical bar in panel (**b**). (**e**) Spatial profile of 1-cycle-per-day period fluctuations of voltage difference time-series at arbitrary time t2 depicted by the black vertical bar in panel (**a**). (**f**) Spatial profile of 1-cycle-per-day period

fluctuations of electric potential time-series at arbitrary time t2 depicted by the black vertical bar in panel (**b**). Colors indicate the spatial position of the measured time-series in the SP electrode array, and correspond to numbered SP electrodes depicted in Figure 5.

The spatial propagation of the transient electric potential wave depicted in Figure 18d,f is indicated by the time delays between the peaks and troughs of diurnal electrical potential fluctuations shown in Figure 18b. Time delays between peaks and troughs of the wave across the SP electrode array were quantified by computing the discrete cross-correlation functions between electric potential fluctuations at electrodes 3–30 and fluctuations at electrode 2. Electrode 1 was not considered because it was used as the global reference for the SP monitoring array and was a zero reference condition. Cross-correlation represents the similarity of two signals quantitatively through the correlation between one signal and a time-delayed copy of the second, expressed as a function of the time delay. Cross-correlations between diurnal electric potential fluctuations were computed with Equation (9) for monitoring data acquired in the pre-streamflow, streamflow, and post-streamflow monitoring periods and are shown in Figure 19a,c,e, respectively. In Equation (9), $R_{k,2}(m)$ is the discrete cross-correlation between data at electrodes k = 3,…, 30 and electrode 2, as a function of time delay m; n = 1,…, N is an index for the discrete sequence of N diurnal electric potential fluctuations; $\bar{V}_2[n]$ is the complex conjugate of diurnal fluctuations at electrode 2; and $V_k[n+m]$ is a shifted sequence of diurnal electric potential fluctuations at electrode k, shifted by a time delay of m samples.

$$R_{k,2}(m) = \begin{cases} \sum_{n=0}^{N-m-1} V_k[n+m] * \bar{V}_2[n] & m \geq 0 \\ \bar{R}_{2,k}[-m] & m < 0 \end{cases} \quad (9)$$

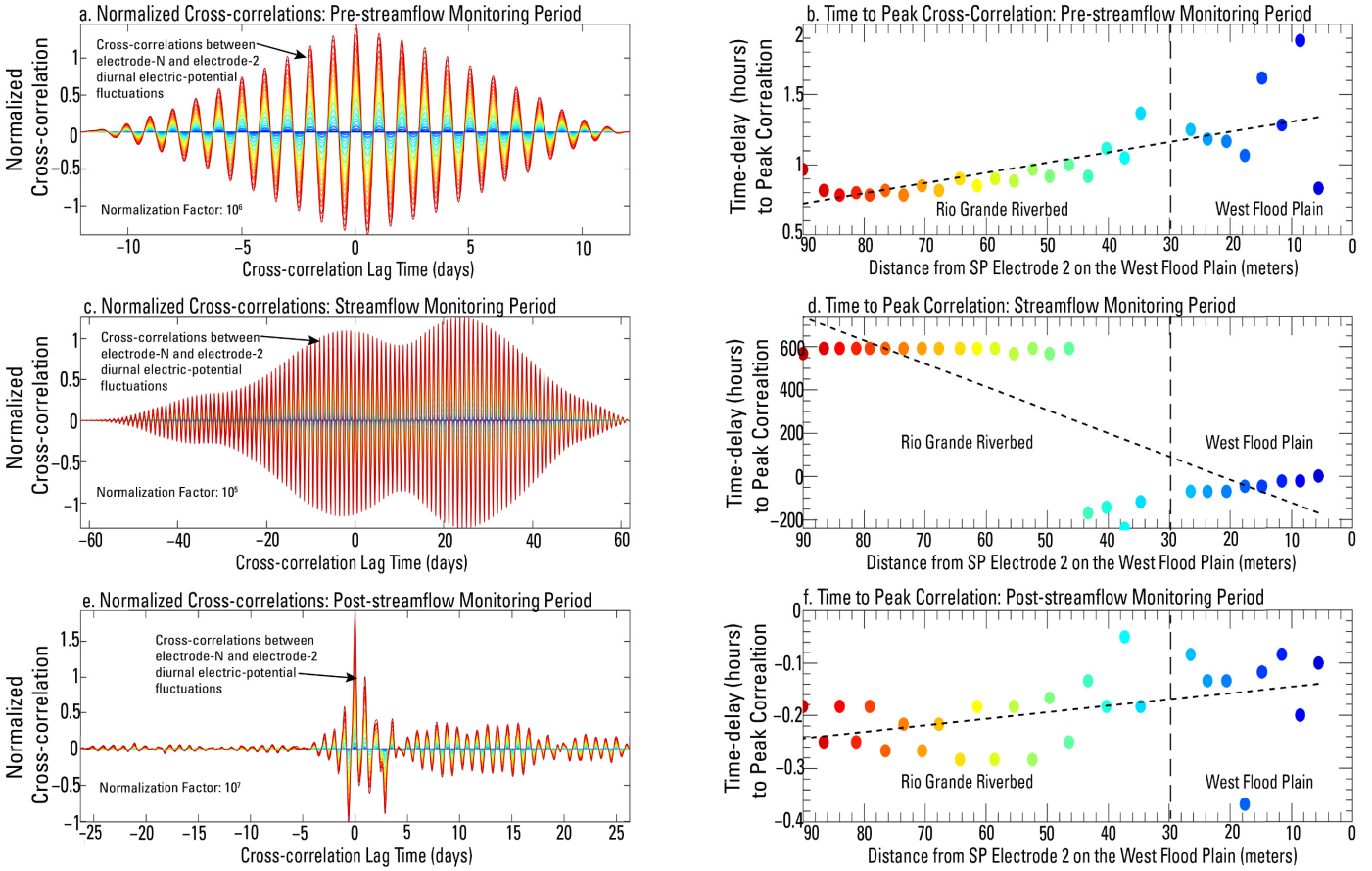

Figure 19. Cross-correlations of diurnal electric potential fluctuations at electrodes 3–30 with diurnal fluctuations at electrode 2 for the pre-streamflow background, streamflow, and post-streamflow monitoring periods showing cross-correlations between time-series as a function of cross-

correlation lag time. (**a**) Cross-correlation functions corresponding to the pre-streamflow background monitoring period. (**b**) Plot of time delay associated with peak cross-correlation between the diurnal electric potential fluctuations (**a**), as a function of distance from electrode 2. (**c**) Cross-correlation functions corresponding to the streamflow monitoring period. (**d**) Plot of time delay associated with peak cross-correlation between the diurnal electric potential fluctuations (**c**), as a function of distance from electrode 2. (**e**) Cross-correlation functions corresponding to the post-streamflow monitoring period. (**f**) Plot of time delay associated with peak cross-correlation between the diurnal electric potential fluctuations (**e**), as a function of distance from electrode 2. Colors indicate the spatial position of the measured time-series in the SP electrode array, and correspond to numbered SP electrodes depicted in Figure 5.

The time delays corresponding to the maximum cross-correlations in Figure 19 indicate the point in time where two cross-correlated signals are the most aligned and therefore the most similar. For highly correlated V_k and V_2, the maximum correlation occurs at a particular time delay of m samples and indicates that a feature in V_2 at time $t_2 = n\mathrm{T}$ also occurs later in V_k at time $t_k = m\mathrm{T}$, where T is the sampling period (60 s) of the diurnal electric potential fluctuations. In other words, V_k could be described to be time-delayed from V_2 by m measurements in time. The time delays associated with the maximum correlations between diurnal electric potential fluctuations at electrodes 3–30 and fluctuations at electrode 2 are plotted as a function of distance from electrode 2 along the self-potential electrode array in Figure 19b,d,f, corresponding to the pre-streamflow, streamflow, and post-streamflow monitoring periods, respectively. Clear differences are evident between each of the three monitoring periods. Time delays between cross-correlated fluctuations at electrode k and electrode 2 are in the range of 0.8–3.3 h during the pre-streamflow monitoring period and show a linear change spatially along the SP electrode array. These time delays are comparable to those in the post-streamflow monitoring period (Figure 19f), which show a similar spatial trend and are generally between about 0.1 and 0.4 h in absolute value. In contrast, the time delays for peak cross-correlations during the streamflow monitoring period show a much different trend than both the pre-streamflow and post-streamflow monitoring periods, with a clear distinction between fluctuations measured at electrodes on the west flood plain and fluctuations measured at electrodes installed in the riverbed. Electrodes on the west flood plain show a linear pattern in time delays relative to electrode 2, whereas the time delays corresponding to riverbed electrodes are much larger during the streamflow monitoring period and show time delays of about 600 h, and the increased time is likely attributed to heat loss by SW advection.

4.6. Practical Implications for Geoelectric Monitoring of Rivers

The methods and data described herein illustrate salient practical aspects of geoelectric monitoring of rivers for better managing limited water resources in arid and semi-arid environments in the face of uncertain future climate change. First, a comparison of the [53] streaming potential profile (Figure 2, black curve) to the electric potential profile shown in Figure 14d is a practical matter that warrants consideration. The location of the monitoring site is indicated on the [53] streaming potential profile and on the location map in Figure 1 relative to the 2010–2011 GW-level differences between the alluvial aquifer and the Santa Fe Group published by [52]. The GW-level differences color-shaded in Figures 1 and 2 indicate that the 2010–2011 vertical hydraulic gradient was such that the lower Rio Grande was losing at the monitoring site in 2010–2011 when GW-level measurements were made. This is consistent with the streaming potential profile in Figure 14d, which shows a losing condition in the river during the streamflow monitoring period. In contrast, the [53] electric potential profile shows a positive electric potential anomaly at the monitoring site. In the context of streaming potential, this positive anomaly was interpreted in agreement with published numerical models of [53,76–78] as indicative of a gaining condition consistent with the relative median gain/loss curve that [52] processed from the [57] seepage data, which also shows a long-term median condition of SW gains between seepage stations S17 and S21; however, the gaining hydraulic condition indicated

by the [53,57] data contradicts the losing conditions at the monitoring site demonstrated herein by the electric potential profile shown in Figure 14d and corroborated by the GW-level differences mapped in Figure 1. One plausible explanation for the discrepancy between these contradictory datasets is that the electric potential profile shown in Figure 14d and the vertical hydraulic gradients inferred from color-coded GW-level differences depicted in Figure 1 represent a state relative to a condition in time, whereas the [57] seepage curve and the [53] electric potential profiles shown in Figure 2 both represent conditions relative to a common point in space. The [57] seepage curve shows gain or loss at a station by an increase or decrease relative to the adjacent upstream station rather than simply in terms of the positive or negative value of their measured seepage data. Thus, the interpretation of gain or loss along any segment of the Rio Grande between the [57] seepage data is relative to the upstream adjacent station, and the net gain or loss at any seepage station is relative to the reference station S01 just downstream from Leasburg Dam (Figure 1). Similarly, the [53] electric potential profile is relative to the same approximate location beginning just downstream from Leasburg Dam such that a relative gaining condition at the monitoring site indicated by the [53] data is relative to the condition at the profile starting point and reflects gains or losses with respect to that reference. This explanation is also plausible with respect to the substantial differences in amplitudes of the electric potential anomalies measured by the [53] data and the current study. Data published by [53] show an electric potential value of about +10 mV at the monitoring site location, whereas the minimum amplitude of the electric potential anomaly shown in the profile in Figure 14d achieves a value of about −3500 mV. The general condition at the monitoring site for the monitoring period is a losing condition, but at this location, the Rio Grande likely has experienced a net gain in streamflow from the aquifer relative to the location of seepage station S01 near Leasburg Dam (Figure 1).

Finally, geoelectric monitoring can be performed along cross-sections of rivers to study time-lapse variability in SW and GW exchanges and hydraulic connectivity between rivers and alluvial aquifers. Using current (2023) data logging and telemetry instrumentation, SP and ERT electrode monitoring arrays can be installed at multiple locations on or within riverbeds to monitor time-lapse changes in hydraulic connectivity and gaining and losing conditions spatially along river segments targeted for scientific investigation. Geoelectric monitoring data can be acquired at high temporal sampling rates and telemetered in near real-time to a remote desktop for data processing and analysis, archival, and interpretation of the spatiotemporal changes in hydraulic connectivity and gaining and losing conditions. The works of [6,11,53] illustrate the relative ease by which long river segments can be monitored and characterized and outline a data-processing and analysis framework for geoelectric monitoring data acquired in future efforts. Improvements in future applications could include the inclusion of fiber-optic-distributed temperature sensing coincident with the geoelectric monitoring profiles, measurement of streamflow and water quality properties upstream and downstream from the monitoring locations, laboratory determination of streaming potential and thermoelectric coupling coefficients for quantitative analysis of water and heat fluxes through the riverbed, and inverse modeling of the electric potential profile data to map the spatiotemporal distributions of streaming potential and thermoelectric sources within the riverbed, support the interpretations, and assess the inherent uncertainty.

5. Conclusions

Time-lapse geoelectric monitoring was performed between 21 May and 4 October 2022 along two cross-sections of the lower Rio Grande riverbed and its west flood plain by using SP monitoring and time-lapse ERT to study the transient changes in hydraulic connection between the Rio Grande and the Rio Grande alluvial aquifer. SP monitoring was performed to measure the changes in the local electric potential field during the transition from dry conditions in the riverbed to bank-full flow conditions and back to dry conditions again. ERT was performed at key times during the SP monitoring survey to

capture transient changes in the subsurface resistivity as the streamflow arrived at the monitoring site and infiltrated into the riverbed.

The geoelectric monitoring data were interpreted in the context of the hydraulic connectivity between the Rio Grande and the alluvial aquifer through comparison of auxiliary time-series data including seepage data from 21 years of annual streamflow gaging surveys; GW levels mapped in 2010–2011 in the alluvial aquifer and the Santa Fe Group; waterborne SP logging surveys completed in 2020; resistivity data acquired from multiple geophysical methods over the course of several decades; weather data including time-series of surface air temperature, soil temperature, precipitation, relative humidity, vapor pressure, barometric pressure, net incident solar radiation, and potential evaporation; and time-series GW-level and streamflow hydrographs monitored near the geoelectric monitoring site during the monitoring period. Percent changes in resistivity determined from ERT data during the streamflow arrival monitoring period indicate that the percent change in resistivity attributed to the presence of SW infiltration into the riverbed occurs rapidly, showing SW infiltration to depths of 3–4 meters in a matter of 4–5 h after streamflow arrival, and indicate that the lower Rio Grande varies from hydraulic disconnection to transitional to hydraulic connection with the alluvial aquifer in a comparable period of time. Self-potential monitoring data acquired during the post-streamflow monitoring period indicate that the progression from hydraulic connection to transitional (between connection and disconnection) to hydraulic disconnection is likely a substantially slower process. GW withdrawal and irrigation on the east flood plain likely draw down the GW table and withdraw more SW from the river on the east bank as indicated by the streaming potential component of the data, growing progressively more negative in magnitude from the west flood plain towards the east bank during periods of streamflow in the river. The streaming potential time-series reflects the fact that the river at the monitoring site is entirely a losing river during the irrigation season when streamflow is present in the river.

The geophysical, hydrologic, and hydraulic datasets analyzed in this study support the conclusion that three different types of electric potentials were measured during the distinct monitoring periods described herein. These three types of potentials directly reflect different hydrologic processes occurring in the Mesilla Basin of southeast New Mexico and are (1) an apparent diffusion potential with an amplitude that varies through time but achieves a maximum of about +100 mV during the pre-streamflow background monitoring period, (2) a streaming potential that is present during the streamflow and post-streamflow monitoring periods and that has an amplitude that grows progressively more negative in time to a minimum value of about −3500 mV, and (3) a thermoelectric potential that varies with a diurnal periodicity and achieves a maximum amplitude of about 40,000–90,000 mV in absolute value daily. The hydrologic processes of saline GW upwelling, SW-GW exchange and river–aquifer connectivity between the lower Rio Grande and the alluvial aquifer, and near-surface heat conduction are directly observed by the time-lapse changes in the electric potential profile across the lower Rio Grande riverbed from the geophysical data through the signal processing approach described in Section 3 and corroborated by previous geophysical, geochemical, and hydrological datasets produced from studies of the lower Rio Grande in the Mesilla Basin and the hydrographic and weather datasets acquired as a part of this geoelectric monitoring survey.

Author Contributions: Conceptualization, S.J.I., A.P.T., K.C.C. and D.F.R.; Methodology, S.J.I., K.C.C. and D.F.R.; Software, S.J.I. and D.F.R.; Validation, S.J.I., A.P.T., K.C.C. and D.F.R.; Formal analysis, S.J.I. and D.F.R.; Investigation, S.J.I., K.C.C. and D.F.R.; Resources, S.J.I., A.P.T., J.D.P., C.-H.T., K.C.C., A.J., D.F.R. and E.H.F.; Data curation, S.J.I., C.-H.T., D.F.R. and E.H.F.; Writing—original draft preparation, S.J.I.; Writing—review and editing, S.J.I., K.C.C. and E.H.F.; Visualization, S.J.I. and D.F.R.; Supervision, S.J.I., A.P.T. and K.C.C.; Project administration, A.P.T.; Funding acquisition, A.P.T. All authors have read and agreed to the published version of the manuscript.

Funding: This research was supported by the U.S. Geological Survey. In-kind services were provided by New Mexico State University (NMSU), Elephant Butte Irrigation District (EBID), and hydroGEOPHYSICS, Inc. (HGI).

Data Availability Statement: The weather, hydrographic, electric resistivity tomography, and self-potential monitoring data, in addition to data-processing codes, photos, and video of streamflow arrival at the geoelectric monitoring site, are available at: https://doi.org/10.5066/P9TBK3NT.

Acknowledgments: The authors wish to thank Armando Alejo and Adam Carrejo at Elephant Butte Irrigation District and David Dubois at New Mexico State University for providing historical weather data, and hydrologic technicians Eric Suh and Marianna Lopez of the U.S. Geological Survey Oklahoma-Texas Water Science Center El Paso field office for assistance with data collection and site maintenance. The authors wish to thank the peer reviewers for their assistance in improving this manuscript. Any use of trade, firm, or product names is for descriptive purposes only and does not imply endorsement by the U.S. Government.

Conflicts of Interest: The authors declare no conflict of interest.

Appendix A. Calculation of Potential Evaporation from Time-Series Weather Data

The [67] combination model, shown in Equation (A1), combines a weighted estimate of potential evaporation attributed to near-surface energy balance variables and the aerodynamic mass flux of water vapor from the land surface [70–72], where E_c (m/day) represents the weighted potential evaporation rate [70], E_r (m/day) represents the potential evaporation rate computed from energy budget calculations [81–83], and E_a (m/day) represents the potential evaporation due to aerodynamic vapor transport processes [84–86]. The weighting coefficients between energy budget and aerodynamic evaporation terms are the psychrometric constant, γ (kPa/K), and the slope of the saturation–vapor pressure curve, Δ (kPa/K) [1,70,71,83]. The energy balance component of evaporation was calculated as an empirical function of net radiation as shown in Equation (A2) [83] (in units of m/day, where R_N is net solar radiation in units of kW/m^2) because the necessary latent and sensible heat-flux measurements required to use energy balance equations were not available.

$$E_c = \frac{\Delta}{\gamma + \Delta} E_r + \frac{\gamma}{\gamma + \Delta} E_a \quad \text{(A1)}$$

$$E_r = 3.53 \times 10^{-5} * R_N \quad \text{(A2)}$$

The psychrometric constant was calculated from Equation (A3), where P_{atm} (kPa) represents barometric pressure, C_a (MJ/kg·K) represents the specific heat capacity of air, and λ_v (MJ/kg) represents the latent heat of vaporization [83], which is calculated as a linear function of surface air temperature as shown in Equation (A4).

$$\gamma = \frac{C_a P_{atm}}{0.622 \lambda_v} \quad \text{(A3)}$$

$$\lambda_v = 2.5 - 0.00236 * T_s \quad \text{(A4)}$$

The slope of the saturation vapor pressure versus surface temperature relationship has been shown to be approximated well by Equation (A5), where T_s (°C) is surface air temperature [83,87].

$$\Delta = \frac{2508.3}{(T_a + 273.3)^2} e \left[\frac{17.27 T_a}{273.3 + T_a}\right] \quad \text{(A5)}$$

The potential evaporation attributed to aerodynamic mass flux was calculated with Equation (A6), where V_w (m/s) represents the mean wind speed measured at height z_2 (meters above the land surface), z_o (m) represents the surface roughness height or vegetative canopy height, P_v (kPa) is the vapor pressure, and $P_{v,sat}$ (kPa) is the saturation

vapor pressure. The roughness height of surface vegetation at the location of the weather station was assumed to be 3 inches.

$$E_a = \frac{1.02 \times 10^{-4} V_w}{\left[ln\left({}^{z_2}/_{z_o}\right)\right]^2} e\left[P_{v,sat} - P_v\right] \quad \text{(A6)}$$

The quantity $[P_{v,sat} - P_v]$ in Equation (A5) is the vapor pressure deficit between the evaporating surface and the surrounding air, and it is due to this term that the [67] combination model gives potential evaporation. Incorporating the saturated vapor pressure assumes that the evaporating surface is completely saturated such that evaporation can progress at the maximum potential rate. Because the saturation vapor pressure variable is unknown at the monitoring site, the term representing saturated vapor pressure is replaced with the actual partial vapor pressure of water in the air, P_a (kPa), which is calculated with Equation (A7) from relative humidity and temperature time-series, where R_h (decimal percent) represents relative humidity [87].

$$P_a = R_h * 0.611e\left[\frac{17.27T_a}{237.3+T_a}\right] \quad \text{(A7)}$$

References

1. Brunner, P.; Cook, P.G.; Simmons, C.T. Hydrogeologic Controls on Disconnection between Surface Water and Groundwater: Hydrogeologic Controls on the Disconnect. *Water Resour. Res.* **2009**, *45*, 1–13. https://doi.org/10.1029/2008WR006953.
2. Brunner, P.; Cook, P.G.; Simmons, C.T. Disconnected Surface Water and Groundwater: From Theory to Practice. *Ground Water* **2011**, *49*, 460–467. https://doi.org/10.1111/j.1745-6584.2010.00752.x.
3. McCallum, A.M.; Andersen, M.S.; Giambastiani, B.M.S.; Kelly, B.F.J.; Ian Acworth, R. River-Aquifer Interactions in a Semi-Arid Environment Stressed by Groundwater Abstraction: River-Aquifer Interactions in a Semi-Arid Environment. *Hydrol. Process.* **2013**, *27*, 1072–1085. https://doi.org/10.1002/hyp.9229.
4. Lamontagne, S.; Taylor, A.R.; Cook, P.G.; Crosbie, R.S.; Brownbill, R.; Williams, R.M.; Brunner, P. Field Assessment of Surface Water-Groundwater Connectivity in a Semi-Arid River Basin (Murray-Darling, Australia). *Hydrol. Process.* **2014**, *28*, 1561–1572. https://doi.org/10.1002/hyp.9691.
5. Fuchs, E.H.; Carroll, K.C.; King, J.P. Quantifying Groundwater Resilience through Conjunctive Use for Irrigated Agriculture in a Constrained Aquifer System. *J. Hydrol.* **2018**, *565*, 747–759. https://doi.org/10.1016/j.jhydrol.2018.08.003.
6. Fuchs, E.H.; King, J.P.; Carroll, K.C. Quantifying Disconnection of Groundwater From Managed-Ephemeral Surface Water During Drought and Conjunctive Agricultural Use. *Water Resour. Res.* **2019**, *55*, 5871–5890. https://doi.org/10.1029/2019WR024941.
7. Sophocleous, M. Interactions between Groundwater and Surface Water: The State of the Science. *Hydrogeol. J.* **2002**, *10*, 52–67. https://doi.org/10.1007/s10040-001-0170-8.
8. Winter, T.C.; Harvey, J.W.; Franke, O.L.; Alley, W.M., *Groundwater and Surface Water: A Single Resource*; U.S. Geological Survey Circular 1139: Reston, VA, USA, 1998; pp. 1–88. https://doi.org/10.3133/cir1139.
9. Brunner, P.; Therrien, R.; Renard, P.; Simmons, C.T.; Franssen, H.-J.H. Advances in Understanding River-Groundwater Interactions: River-Groundwater Interactions. *Rev. Geophys.* **2017**, *55*, 818–854. https://doi.org/10.1002/2017RG000556.
10. Banks, E.W.; Simmons, C.T.; Love, A.J.; Shand, P. Assessing Spatial and Temporal Connectivity between Surface Water and Groundwater in a Regional Catchment: Implications for Regional Scale Water Quantity and Quality. *J. Hydrol.* **2011**, *404*, 30–49. https://doi.org/10.1016/j.jhydrol.2011.04.017.
11. Pearson, A.J.; Rucker, D.F.; Tsai, C.-H.; Fuchs, E.H.; Carroll, K.C. Electrical Resistivity Monitoring of Lower Rio Grande River-Groundwater Intermittency. *J. Hydrol.* **2022**, *613*, 128325. https://doi.org/10.1016/j.jhydrol.2022.128325.
12. Wroblicky, G.J.; Campana, M.E.; Valett, H.M.; Dahm, C.N. Seasonal Variation in Surface-Subsurface Water Exchange and Lateral Hyporheic Area of Two Stream-Aquifer Systems. *Water Resour. Res.* **1998**, *34*, 317–328. https://doi.org/10.1029/97WR03285.
13. Shanafield, M.; Cook, P.G. Transmission Losses, Infiltration and Groundwater Recharge through Ephemeral and Intermittent Streambeds: A Review of Applied Methods. *J. Hydrol.* **2014**, *511*, 518–529. https://doi.org/10.1016/j.jhydrol.2014.01.068.
14. Gutiérrez-Jurado, K.Y.; Partington, D.; Batelaan, O.; Cook, P.; Shanafield, M. What Triggers Streamflow for Intermittent Rivers and Ephemeral Streams in Low-Gradient Catchments in Mediterranean Climates. *Water Resour. Res.* **2019**, *55*, 9926–9946. https://doi.org/10.1029/2019WR025041.
15. Messager, M.L.; Lehner, B.; Cockburn, C.; Lamouroux, N.; Pella, H.; Snelder, T.; Tockner, K.; Trautmann, T.; Watt, C.; Datry, T. Global Prevalence of Non-Perennial Rivers and Streams. *Nature* **2021**, *594*, 391–397. https://doi.org/10.1038/s41586-021-03565-5.
16. McLachlan, P.J.; Chambers, J.E.; Uhlemann, S.S.; Binley, A. Geophysical Characterisation of the Groundwater–Surface Water Interface. *Adv. Water Resour.* **2017**, *109*, 302–319. https://doi.org/10.1016/j.advwatres.2017.09.016.
17. Nyquist, J.E.; Corry, C.E. Self-Potential: The Ugly Duckling of Environmental Geophysics. *Lead. Edge* **2002**, *21*, 446–451. https://doi.org/10.1190/1.1481251.

18. Ernstson, K.; Scherer, H.U. Self-potential Variations with Time and Their Relation to Hydrogeologic and Meteorological Parameters. *Geophysics* **1986**, *51*, 1967–1977. https://doi.org/10.1190/1.1442052.
19. Perrier, F.E.; Petiau, G.; Clerc, G.; Bogorodsky, V.; Erkul, E.; Jouniaux, L.; Lesmes, D.; Macnae, J.; Meunier, J.M.; Morgan, D.; et al. A One-Year Systematic Study of Electrodes for Long Period Measurements of the Electric Field in Geophysical Environments. *J. Geomagn. Geoelectr.* **1997**, *49*, 1677–1696. https://doi.org/10.5636/jgg.49.1677.
20. Perrier, F.; Pant, S.R. Noise Reduction in Long-Term Self-Potential Monitoring with Travelling Electrode Referencing. *Pure Appl. Geophys.* **2005**, *162*, 165–179. https://doi.org/10.1007/s00024-004-2585-3.
21. Perrier, F.; Trique, M.; Aupiais, J.; Gautam, U.; Shrestha, P. Electric Potential Variations Associated with Periodic Spring Discharge in Western Nepal. *Comptes Rendus De L'académie Des Sci. Ser. IIA Earth Planet. Sci.* **1999**, *328*, 73–79. https://doi.org/10.1016/S1251-8050(99)80001-9.
22. Perrier, F.; Morat, P. Characterization of Electrical Daily Variations Induced by Capillary Flow in the Non-Saturated Zone: *Pure Appl. Geophys.* **2000**, *157*, 785–810. https://doi.org/10.1007/PL00001118.
23. Gibert, D.; Le Mouël, J.-L.; Lambs, L.; Nicollin, F.; Perrier, F. Sap Flow and Daily Electric Potential Variations in a Tree Trunk. *Plant Sci.* **2006**, *171*, 572–584. https://doi.org/10.1016/j.plantsci.2006.06.012.
24. Crespy, A.; Revil, A.; Linde, N.; Byrdina, S.; Jardani, A.; Bolève, A.; Henry, P. Detection and Localization of Hydromechanical Disturbances in a Sandbox Using the Self-Potential Method. *J. Geophys. Res. Solid Earth* **2008**, *113*, B01205. https://doi.org/10.1029/2007JB005042.
25. Ikard, S.J.; Revil, A.; Jardani, A.; Woodruff, W.F.; Parekh, M.; Mooney, M. Saline Pulse Test Monitoring with the Self-Potential Method to Nonintrusively Determine the Velocity of the Pore Water in Leaking Areas of Earth Dams and Embankments. *Water Resour. Res.* **2012**, *48*, W04201. https://doi.org/10.1029/2010WR010247.
26. Ikard, S.J.; Revil, A. Self-Potential Monitoring of a Thermal Pulse Advecting through a Preferential Flow Path. *J. Hydrol.* **2014**, *519*, 34–49. https://doi.org/10.1016/j.jhydrol.2014.07.001.
27. Voytek, E.B.; Barnard, H.R.; Jougnot, D.; Singha, K. Transpiration- and Precipitation-induced Subsurface Water Flow Observed Using the Self-potential Method. *Hydrol. Process.* **2019**, *33*, 1784–1801. https://doi.org/10.1002/hyp.13453.
28. Fernandez, P.M.; Bloem, E.; Binley, A.; Philippe, R.S.B.A.; French, H.K. Monitoring Redox Sensitive Conditions at the Groundwater Interface Using Electrical Resistivity and Self-Potential. *J. Contam. Hydrol.* **2019**, *226*, 103517. https://doi.org/10.1016/j.jconhyd.2019.103517.
29. Doro, K.O.; Stoikopoulos, N.P.; Bank, C.-G.; Ferris, F.G. Self-Potential Time Series Reveal Emergent Behavior in Soil Organic Matter Dynamics. *Sci. Rep.* **2022**, *12*, 13531. https://doi.org/10.1038/s41598-022-17914-5.
30. Loke, M.H.; Chambers, J.E.; Rucker, D.F.; Kuras, O.; Wilkinson, P.B. Recent Developments in the Direct-Current Geoelectrical Imaging Method. *J. Appl. Geophys.* **2013**, *95*, 135–156. https://doi.org/10.1016/j.jappgeo.2013.02.017.
31. Rucker, D. A Coupled Electrical Resistivity-Infiltration Model for Wetting Front Evaluation. *Vadose Zone J.* **2009**, *8*, 383–388. https://doi.org/10.2136/vzj2008.0080.
32. Blazevic, L.; Bodet, L.; Pasquet, S.; Linde, N.; Jougnot, D.; Longuevergne, L. Time-Lapse Seismic and Electrical Monitoring of the Vadose Zone during a Controlled Infiltration Experiment at the Ploemeur Hydrological Observatory, France. *Water* **2020**, *12*, 1230. https://doi.org/10.3390/w12051230.
33. Hilbich, C. Time-Lapse Refraction Seismic Tomography for the Detection of Ground Ice Degradation. *Cryosphere* **2010**, *4*, 243–259. https://doi.org/10.5194/tc-4-243-2010.
34. Hauck, C. Frozen Ground Monitoring Using DC Resistivity Tomography. *Geophys. Res. Lett.* **2002**, *29*, 2016. https://doi.org/10.1029/2002GL014995.
35. Sjödahl, P.; Dahlin, T.; Johansson, S.; Loke, M.H. Resistivity Monitoring for Leakage and Internal Erosion Detection at Hällby Embankment Dam. *J. Appl. Geophys.* **2008**, *65*, 155–164. https://doi.org/10.1016/j.jappgeo.2008.07.003.
36. Sjödahl, P.; Dahlin, T.; Johansson, S. Embankment Dam Seepage Evaluation from Resistivity Monitoring Data. *Near Surf. Geophys.* **2009**, *7*, 463–474. https://doi.org/10.3997/1873-0604.2009023.
37. Rucker, D.F.; Fink, J.B.; Loke, M.H. Environmental Monitoring of Leaks Using Time-Lapsed Long Electrode Electrical Resistivity. *J. Appl. Geophys.* **2011**, *74*, 242–254. https://doi.org/10.1016/j.jappgeo.2011.06.005.
38. Slater, L.D.; Sandberg, S.K. Resistivity and Induced Polarization Monitoring of Salt Transport under Natural Hydraulic Gradients. *Geophysics* **2000**, *65*, 408–420. https://doi.org/10.1190/1.1444735.
39. Trento, L.M.; Tsourlos, P.; Gerhard, J.I. Time-Lapse Electrical Resistivity Tomography Mapping of DNAPL Remediation at a STAR Field Site. *J. Appl. Geophys.* **2021**, *184*, 104244. https://doi.org/10.1016/j.jappgeo.2020.104244.
40. Acworth, R.I.; Dasey, G.R. Mapping of the Hyporheic Zone around a Tidal Creek Using a Combination of Borehole Logging, Borehole Electrical Tomography and Cross-Creek Electrical Imaging, New South Wales, Australia. *Hydrogeol. J.* **2003**, *11*, 368–377. https://doi.org/10.1007/s10040-003-0258-4.
41. Mansoor, N.; Slater, L. Aquatic Electrical Resistivity Imaging of Shallow-Water Wetlands. *Geophysics* **2007**, *72*, F211–F221. https://doi.org/10.1190/1.2750667.
42. Crook, N.; Binley, A.; Knight, R.; Robinson, D.A.; Zarnetske, J.; Haggerty, R. Electrical Resistivity Imaging of the Architecture of Substream Sediments. *Water Resour. Res.* **2008**, *44*, W00D13. https://doi.org/10.1029/2008WR006968.
43. Nyquist, J.E.; Freyer, P.A.; Toran, L. Stream Bottom Resistivity Tomography to Map Ground Water Discharge. *Ground Water* **2008**, *46*, 561–569. https://doi.org/10.1111/j.1745-6584.2008.00432.x.

44. Singha, K.; Pidlisecky, A.; Day-Lewis, F.D.; Gooseff, M.N. Electrical Characterization of Non-Fickian Transport in Groundwater and Hyporheic Systems. *Water Resour. Res.* **2008**, *44*, W00D07. https://doi.org/10.1029/2008WR007048.
45. Musgrave, H.; Binley, A. Revealing the Temporal Dynamics of Subsurface Temperature in a Wetland Using Time-Lapse Geophysics. *J. Hydrol.* **2011**, *396*, 258–266. https://doi.org/10.1016/j.jhydrol.2010.11.008.
46. Ward, A.S.; Gooseff, M.N.; Singha, K. Imaging Hyporheic Zone Solute Transport Using Electrical Resistivity. *Hydrol. Process.* **2010**, *24*, 948–953. https://doi.org/10.1002/hyp.7672.
47. Koehn, W.J.; Tucker-Kulesza, S.E.; Steward, D.R. Conceptualizing Groundwater-Surface Water Interactions within the Ogallala Aquifer Region Using Electrical Resistivity Imaging. *J. Environ. Eng. Geophys.* **2019**, *24*, 185–199. https://doi.org/10.2113/JEEG24.2.185.
48. Koehn, W.J.; Tucker-Kulesza, S.E.; Steward, D.R. Characterizing Streambed Heterogeneity across Shifts in River Discharge through Temporal Changes in Electrical Resistivity. *J. Environ. Eng. Geophys.* **2020**, *25*, 581–587. https://doi.org/10.32389/JEEG20-049.
49. McLachlan, P.; Chambers, J.; Uhlemann, S.; Sorensen, J.; Binley, A. Electrical Resistivity Monitoring of River–Groundwater Interactions in a Chalk River and Neighboring Riparian Zone. *Near Surf. Geophys.* **2020**, *18*, 385–398. https://doi.org/10.1002/nsg.12114.
50. Shanafield, M.; Gutiérrrez-Jurado, K.; White, N.; Hatch, M.; Keane, R. Catchment-Scale Characterization of Intermittent Stream Infiltration; a Geophysics Approach. *J. Geophys. Res. Earth Surf.* **2020**, *125*, e2019JF005330. https://doi.org/10.1029/2019JF005330.
51. Rucker, D.F.; Tsai, C.-H.; Carroll, K.C.; Brooks, S.; Pierce, E.M.; Ulery, A.; Derolph, C. Bedrock Architecture, Soil Texture, and Hyporheic Zone Characterization Combining Electrical Resistivity and Induced Polarization Imaging. *J. Appl. Geophys.* **2021**, *188*, 104306. https://doi.org/10.1016/j.jappgeo.2021.104306.
52. Teeple, A.P. *Geophysics and Geochemistry-Based Assessment of the Geochemical Characteristics and Groundwater-Flow System of the U.S. Part of the Mesilla Basin/Conejos-Médanos Aquifer System in Doña Ana County, New Mexico, and El Paso County, Texas, 2010–2012*; Scientific Investigations Report 2017–5028; U.S. Geological Survey: Reston, VA, USA, 2017; pp. 1–183. https://doi.org/10.3133/sir20175028.
53. Ikard, S.; Teeple, A.; Humberson, D. Gradient Self-Potential Logging in the Rio Grande to Identify Gaining and Losing Reaches across the Mesilla Valley. *Water* **2021**, *13*, 1331. https://doi.org/10.3390/w13101331.
54. Robertson, A.J.; Matherne, A.-M.; Pepin, J.D.; Ritchie, A.B.; Sweetkind, D.S.; Teeple, A.P.; Granados-Olivas, A.; García-Vásquez, A.C.; Carroll, K.C.; Fuchs, E.H.; et al. Mesilla/Conejos-Médanos Basin: U.S.-Mexico Transboundary Water Resources. *Water* **2022**, *14*, 134. https://doi.org/10.3390/w14020134.
55. Phillips, F.M.; Mills, S.; Hendrickx, M.H.; Hogan, J. Environmental Tracers Applied to Quantifying Causes of Salinity in Arid-Region Rivers: Results from the Rio Grande Basin, Southwestern USA. In *Developments in Water Science*; Elsevier BV: Amsterdam, The Netherlands, 2003; Volume 50, pp. 327–334. https://doi.org/10.1016/S0167-5648(03)80029-1.
56. Pepin, J.D.; Robertson, A.J.; Kelley, S.A. Salinity Contributions from Geothermal Waters to the Rio Grande and Shallow Aquifer System in the Transboundary Mesilla (United States)/Conejos-Médanos (Mexico) Basin. *Water* **2021**, *14*, 33. https://doi.org/10.3390/w14010033.
57. Crilley, D.M.; Matherne, A.M.; Thomas, N.; Falk, S.E. *Seepage Investigations of the Rio Grande from below Leasburg Dam, Leasburg, New Mexico, to above American Dam, El Paso, Texas, 2006–2013*; Scientific Investigations Report 2019-5140; U.S. Geological Survey: Reston, VA, USA, 2013; pp. 1–34. https://doi.org/10.3133/sir20195140.
58. Dunbar, J.B.; Murphy, W.L.; Ballard, R.F.; McGill, T.E.; Peyman-Dove, L.D.; Bishop, M.J. *Condition Assessment of U.S. International Boundary and Water Commission, Texas and New Mexico Levees—Report 2*; U.S. Army Corps of Engineers, Engineering Research and Development Center: Vicksburg, MS, USA, 2004; p. 121.
59. Zohdy, A.A.R.; Bisdorf, R.J.; Gates, J.S. *Schlumberger Soundings in the Lower Mesilla Valley of the Rio Grande, Texas and New Mexico*; Open-File Report 76-324; U.S. Geological Survey: Reston, VA, USA, 1976; pp. 1–77. https://doi.org/10.3133/ofr76324.
60. Cubbage, B.; Noonan, G.E.; Rucker, D.F. A Modified Wenner Array for Efficient Use of Eight-Channel Resistivity Meters. *Pure Appl. Geophys.* **2017**, *174*, 2705–2718. https://doi.org/10.1007/s00024-017-1535-9.
61. Dahlin, T.; Zhou, B. Multiple-Gradient Array Measurements for Multichannel 2D Resistivity Imaging. *Near Surf. Geophys.* **2006**, *4*, 113–123. https://doi.org/10.3997/1873-0604.2005037.
62. Dey, A.; Morrison, H.F. Resistivity modeling for arbitrarily shaped two-dimensional structures. *Geophys. Prospect.* **1979**, *27*, 106–136. https://doi.org/10.1111/j.1365-2478.1979.tb00961.x.
63. Loke, M.H.; Barker, R.D. Rapid Least-Squares Inversion of Apparent Resistivity Pseudosections by a Quasi-Newton Method. *Geophys. Prospect.* **1996**, *44*, 131–152. https://doi.org/10.1111/j.1365-2478.1996.tb00142.x.
64. Loke, M.H.; Acworth, I.; Dahlin, T. A Comparison of Smooth and Blocky Inversion Methods in 2D Electrical Imaging Surveys. *Explor. Geophys.* **2003**, *34*, 182–187. https://doi.org/10.1071/EG03182.
65. Kim, J.-H.; Yi, M.-J.; Park, S.-G.; Kim, J.G. 4-D Inversion of DC Resistivity Monitoring Data Acquired over a Dynamically Changing Earth Model. *J. Appl. Geophys.* **2009**, *68*, 522–532. https://doi.org/10.1016/j.jappgeo.2009.03.002.
66. Rucker, D.F.; Crook, N.; Winterton, J.; McNeill, M.; Baldyga, C.A.; Noonan, G.; Fink, J.B. Real-time Electrical Monitoring of Reagent Delivery during a Subsurface Amendment Experiment. *Near Surf. Geophys.* **2014**, *12*, 151–163. https://doi.org/10.3997/1873-0604.2013017.
67. Penman, H.L. Natural Evaporation from Open Water, Bare Soil and Grass. *Proc. R. Soc. A* **1948**, *193*, 120–145. https://doi.org/10.1098/rspa.1948.0037.

68. Businger, J.A. Some Remarks on Penman's Equations for the Evapotranspiration. *NJAS Wagening. J. Life Sci.* **1956**, *4*, 77–80. https://doi.org/10.18174/njas.v4i1.17778.
69. Penman, H.L. Evaporation: An Introductory Survey. *NJAS Wagening. J. Life Sci.* **1956**, *4*, 9–29. https://doi.org/10.18174/njas.v4i1.17768.
70. Van Bavel, C.H.M. Potential Evaporation: The Combination Concept and Its Experimental Verification. *Water Resour. Res.* **1966**, *2*, 455–467. https://doi.org/10.1029/WR002i003p00455.
71. Brutsaert, W. *Evaporation into the Atmosphere*; Springer: Dordrecht, The Netherlands, 1982; ISBN 978-90-481-8365-4.
72. Todd, R.W.; Evett, S.R.; Howell, T.A. The Bowen Ratio-Energy Balance Method for Estimating Latent Heat Flux of Irrigated Alfalfa Evaluated in a Semi-Arid, Advective Environment. *Agric. For. Meteorol.* **2000**, *103*, 335–348. https://doi.org/10.1016/S0168-1923(00)00139-8.
73. Ikard, S.J.; Carroll, K.C.; Rucker, D.F.; Teeple, A.P.; Payne, J.D.; Tsai, C.H.; Fuchs, E.H.; Jamil, A. *Time-Lapse Self-Potential, Electrical Resistivity Tomography, Streamflow, Groundwater-Level, and Climate Datasets Acquired 21 May 2022 through 4 October 2022, in the Lower Rio Grande, Southeastern New Mexico*; U.S. Geological Survey Data Release: Denver, Colorado, 2023. https://doi.org/10.5066/P9TBK3NT.
74. Turnipseed, D.P.; Sauer, V.B. *Discharge Measurements at Gaging Stations*; Techniques and Methods Book 3, Chapter A8; U.S. Geological Survey: Reston, VA, USA, 2010; pp. 1–87. https://doi.org/10.3133/tm3A8.
75. Cunningham, W.L.; Schalk, C.W. *Groundwater Technical Procedures of the U.S. Geological Survey*; Techniques and Methods 1–A1; U.S. Geological Survey: Reston, VA, USA, 2011; pp. 1–151.
76. Valois, R.; Cousquer, Y.; Schmutz, M.; Pryet, A.; Delbart, C.; Dupuy, A. Characterizing Stream-Aquifer Exchanges with Self-Potential Measurements. *Groundwater* **2018**, *56*, 437–450. https://doi.org/10.1111/gwat.12594.
77. Ikard, S.J.; Teeple, A.P.; Payne, J.D.; Stanton, G.P.; Banta, J.R. New Insights on Scale-Dependent Surface-Groundwater Exchange from a Floating Self-Potential Dipole. *J. Environ. Eng. Geophys.* **2018**, *23*, 261–287. https://doi.org/10.2113/JEEG23.2.261.
78. Ikard, S.J.; Briggs, M.A.; Lane, J.W. Investigation of Scale-Dependent Groundwater/Surface-Water Exchange in Rivers by Gradient Self-Potential Logging: Numerical Modeling and Field Experiments. *J. Environ. Eng. Geophys.* **2021**, *26*, 83–98. https://doi.org/10.32389/JEEG20-066.
79. Corwin, R.F.; Hoover, D.B. The Self-potential Method in Geothermal Exploration. *Geophysics* **1979**, *44*, 226–245. https://doi.org/10.1190/1.1440964.
80. Anderson, M.P. Heat as a Ground Water Tracer. *Ground Water* **2005**, *43*, 951–968. https://doi.org/10.1111/j.1745-6584.2005.00052.x.
81. Chow, V.T.; Maidment, D.; Mays, L.W. *Applied Hydrology*; McGraw-Hill: New York, NY, USA, 1988; pp. 1–572.
82. Wang, J.; Salvucci, G.D.; Bras, R.L. An Extremum Principle of Evaporation. *Water Resour. Res.* **2004**, *40*, W09303. https://doi.org/10.1029/2004WR003087.
83. Jury, W.A.; Horton, R. *Soil Physics*, 6th ed.; John Wiley & Sons: Hoboken, NJ, USA, 2004; pp. 1–370.
84. Heine, R.W. Comparison of Monthly Piche Readings with the Penman Aerodynamic Term in the New Zealand Climate Network. *Agric. Meteorol.* **1981**, *25*, 67–74. https://doi.org/10.1016/0002-1571(81)90062-5.
85. Papaioannou, G.; Vouraki, K.; Kerkides, P. Piche Evaporimeter Data as a Substitute for Penman Equation's Aerodynamic Term. *Agric. For. Meteorol.* **1996**, *82*, 83–92. https://doi.org/10.1016/0168-1923(96)02337-4.
86. Fitzpatrick, E.A.; Stern, W.R. Estimates of Potential Evaporation Using Alternative Data in Penman's Formula. *Agric. Meteorol.* **1966**, *3*, 225–239. https://doi.org/10.1016/0002-1571(66)90030-6.
87. Murray, F.W. On the Computation of Saturated Vapor Pressure. *J. Appl. Meteorol.* **1967**, *6*, 203–205. https://doi.org/10.1175/1520-0450(1967)006%3C0203:OTCOSV%3E2.0.CO;2.

Disclaimer/Publisher's Note: The statements, opinions and data contained in all publications are solely those of the individual author(s) and contributor(s) and not of MDPI and/or the editor(s). MDPI and/or the editor(s) disclaim responsibility for any injury to people or property resulting from any ideas, methods, instructions or products referred to in the content.